ARCHIVIO ISTITUZIONALE
DELLA RICERCA

Alma Mater Studiorum Università di Bologna
Archivio istituzionale della ricerca

Combined experimental-numerical study on vortex-induced vibrations of curved cable-stayed bridge: Effects of superelevation and spatial curvature

This is the final peer-reviewed author's accepted manuscript (postprint) of the following publication:

Published Version:
Li, W., Yuan, R., An, Y., Li, X., Niu, H., Patruno, L., et al. (2025). Combined experimental-numerical study on vortex-induced vibrations of curved cable-stayed bridge: Effects of superelevation and spatial curvature. PHYSICS OF FLUIDS, 37(8), 1-18 [10.1063/5.0284282].

Availability:
This version is available at: https://hdl.handle.net/11585/1037255 since: 2026-01-15

Published:
DOI: http://doi.org/10.1063/5.0284282

Terms of use:

Some rights reserved. The terms and conditions for the reuse of this version of the manuscript are specified in the publishing policy. For all terms of use and more information see the publisher's website.

This item was downloaded from IRIS Università di Bologna (https://cris.unibo.it/).
When citing, please refer to the published version.

(Article begins on next page)

07 October 2026

Combined experimental-numerical study on Vortex-induced vibrations of curved cable-stayed bridge: effects of superelevation and spatial curvature

Weilin Li [a,b] (李威霖), Rong Yuan [a,b] (袁蓉), Yonghui An [a,b,c*] (安永辉), Xuejie Li [a,b] (李学杰), Huawei Niu [d] (牛华伟), Luca Patruno [e], Xugang Hua [d] (华旭刚)

[a] School of Civil Engineering and Architecture, Guangxi University, Nanning Guangxi 530004, China

[b] State Key Laboratory of Featured Metal Materials and Life-cycle Safety for Composite Structures (Provincially and Ministerially Co-constructed), Nanning Guangxi 530004, China

[c] Department of Civil Engineering, Dalian University of Technology, Dalian 116023, China

[d] Key Laboratory for Wind and Bridge Engineering of Hunan Province, College of Civil Engineering, Hunan University, Changsha 410082, China

[e] DICAM, University of Bologna, Viale Risorgimento 2, 40136 Bologna, Italy

** Correspondence:* anyh@dlut.edu.cn

Abstracts: The Vortex-Induced Vibrations (VIVs) of curved cable-stayed bridges differ from those of straight bridges due to two key factors. First, the superelevation introduces deck asymmetry and alters effective angle of attack, leading to mechanisms responsible for VIVs that remain unclear. Second, spatial curvature modifies wind yaw angles and induces coupled vertical-torsional VIVs, complicating the mode shape correlation factor (MSCF) and making it challenging to assess VIVs solely from straight sectional model. Investigating these effects through Wind Tunnel Tests (WTTs) requires costly multiple sectional models, while Fluid-Structure Interaction (FSI) simulations of in-service decks demand high computational burdens due to the fine mesh required for modeling barrier configurations. In this study, the effects of superelevation are investigated by combining sectional models WTTs and FSI simulations using two-dimensional (2D) Unsteady Reynolds-Averaged Navier-Stokes (URANS) and three-dimensional (3D) Improved Delayed Detached Eddy Simulation (IDDES). Zero-thickness baffles are employed to model the barriers and accelerate simulations. Furthermore, the spatial curvature effects and MSCF are clarified by comparing sectional and full curved model WTTs. Results show that 2D URANS overestimates VIVs due to inability to capture inner recirculation regions on the deck's lower surface, while 3D IDDES agree well with WTTs. Superelevation has unfavorable effects on VIVs by generating strong secondary vortices downstream of the central barrier at certain yaw angles, leading to conditions which might increase VIV amplitudes with respect to standard decks. The MSCF of 1.28 is recommended for coupled vertical-torsional VIVs, providing practical guidance for evaluating curved bridges VIVs using simplified sectional models.

Key words: Curved cable-stayed bridge; Vortex-induced vibration; Superelevation; Wind tunnel tests; Unsteady Reynolds-averaged Navier-Stokes; Improved Delayed Detached Eddy Simulation.

1. Introduction

Curved Cable-stayed Bridges (CCBs) are increasingly important in modern transportation systems [1]. Examples include Italy's Ponte del Mare bridge (main span 172m), Japan's Katsushika Harp Bridge (220m), France's Térénez bridge (285 m), and the under-construction Bjørnefjorden bridge (450 m) in Norway [2]. As the main span increases, the decrease in stiffness and damping makes these slender structures prone to large-amplitude Vortex-Induced Vibrations (VIVs) during in-service conditions [3-11]. Although VIVs of straight bridges have been comprehensive studied [12-19], VIV characteristics of CCBs are still unclear and require thorough investigations.

The first key feature of a CCB deck that distinguishes VIVs from those of straight bridges is the implementation of superelevation on the upper deck surface. Such transverse inclination is designed to improve vehicle stability and safety by counteracting centrifugal forces experienced during curve traversal. For instance, AASHTO specifications [20] allow superelevation of up to 8% for highway bridges. However from an aerodynamic perspective, this superelevation introduces a deck asymmetry, which might act as an effective wind attack of angle (AOA) and thus impact the VIVs [21-28]. For instance, Wang et al. [29] conducted Wind Tunnel Tests (WTTs) on a bikeway-induced asymmetric deck and found significant differences in the VIV regions and amplitudes between opposite wind directions (0° and 180°). Liu et al. [30-32] studied the pressure distributions and VIV responses of a twin asymmetric separated parallel deck and documented the differences recorded under opposite inflow direction. Stoyanoff et al. [33] also found that for asymmetric cross-section arrangements, solutions for one wind direction may lead to unacceptable results for the other, so both directions need to be tested. Therefore, the influence mechanism of deck asymmetry induced by superelevation on VIVs requires systematic investigations.

Given that the in-service CCB deck has not only superelevation but also barriers or railings that affect flow organizations, investigating VIVs might benefit from sectional model WTTs [34-46] and Computational Fluid Dynamics (CFD) simulations [28, 47-56]. In particular, WTTs are regarded as a reliable method for evaluating the VIVs of bridge deck with barriers [57-64]. For example, Yang et al. [65] found that wind barriers intensify vertical VIV of a triple-box girders, while railway wind

barriers and crash barriers help to mitigate it. Ge et al. [58] investigated VIV-triggering mechanisms for the Humen Bridge due to temporary water-filled barriers. Wu et al. [57] found that flow separation generated on wind barriers and railings significantly amplifies the vortex-induced forces of a triple-box girder. Liu et al. [59] found that varying the height and porosity of barriers modifies the VIV characteristics of a double-deck girder. However, assessing superelevation effects using WTTs requires multiple section models with varying upper surface inclinations, leading to substantial experimental costs. For instance, Yoshimura et al. [66] used five sectional models to obtain the aerodynamic damping of a CCB deck with superelevation rate from 0% to 9% and found that accurate analysis requires results from at least three sectional models. In contrast, CFD-based Fluid-Structure Interaction (FSI) simulations, allowing to easily modify geometrical details, might prove an attractive complementary approach [57-62] to study the effect of superelevation. Nevertheless, the accuracy of CFD for in-service bridge decks are constrained by the high computational costs associated with fine grids around porous barriers [67, 68]. Liu et al. [69] found that two-dimensional (2D) Unsteady Reynolds-Averaged Navier-Stokes Simulations (URANS) perform well for VIV prediction in a bridge deck with barriers, while Huang et al. [70] and Liu et al. [71] found 2D URANS still have limitations in accurately predicting VIV amplitude and lock-in ranges. Notably, 2D FSI may not account for span-wise correlations, and research on VIVs using three-dimensional (3D) FSI simulations for in-service decks remains limited due to the tiny cells around barrier cause a sharp increase in the Courant number. To date, CFD studies on CCB decks with superelevation and barriers are still lacking, and effective strategies are required to reduce computational cost to guide preliminary wind-resistant designs.

Another key feature of CCBs is that the spatial curvature increases complexity of VIVs compared to straight bridges. Such curvature creates a variation of the wind yaw angles along the bridge span [72-74], potentially affecting VIV amplitudes and lock-in regions [75-77]. Furthermore, this curvature introduces coupled bending-torsional behavior, making it difficult to determine VIV amplitudes using only straight sectional model WTTs. As a result, costly full-aeroelastic curved models for WTTs are required [78-81]. To reduce experimental costs, the Mode Shape Correction Factor (MSCF) is often adopted to convert VIV results from a straight sectional to the curved bridge [82]. However, the MSCF value depends on the adopted empirical model used to represent the vortex-

induced force. Assuming perfectly correlated vortex-induced forces and a sinusoidal mode shape, the theoretical MSCF of a straight bridge is $4/\pi$ using Scanlan linear model and $2/\sqrt{3}$ using a non-linear empirical model [83]. Macdonald et al. [84] found that setting the MSCF value at 1.4 allows the sectional model to closely replicate the prototype VIVs of the Second Severn Crossing bridge. Zhou et al. [85] proposed a multi-supported aeroelastic model and found that the experimental MSCF for a 6:1 rectangular cylinder ranges from 1.25 to 1.3. While the MSCF for straight bridges is well-studied, its value for CCBs is unknown, making it difficult to accurately estimate prototype VIVs using simplified sectional models.

From the previous discussion, it clearly emerges that the evaluation of VIVs for CCBs is of great technical importance but present additional difficulties with respect to straight bridges, due to the presence of superelevation and spatial curvature. To systematically study such aspects, this study systematically investigates the VIVs of a CCB through straight section model WTTs, CFD simulations and full curved aeroelastic model WTTs. Firstly, the VIVs of a CCB deck with barriers are investigated by combining sectional model WTTs and FSI simulations based on 2D URANS and 3D IDDES (Improved Delayed Detached Eddy Simulation) [86-89]. Zero-thickness baffles [90] are employed to model the porous barriers and improve FSI efficiency. Subsequently, FSI simulations at opposite inflows (0° and 180°) and varying superelevation rate from 1.5% to 6% are performed to study the influence mechanism of superelevation on VIVs. Finally, the effects of span-wise curves and MSCF are clarified by comparing the results of sectional and full curved model.

This paper is organized as follows: Section 2 presents the WTTs setup for both the sectional and full curved aeroelastic models of the CCB. Section 3 details the numerical settings of the 2D URANS and 3D IDDES. Results are discussed in Section 4, and conclusions are drawn in Section 5.

2. Experimental setup

2.1 Overview of curved cable-stayed bridge

Figure 1 presents the elevation view, plan view and cross-section of the considered CCB. The bridge has a total length of 408 m with four spans (50 m + 96 m + 192 m + 70 m), and the main span covers a distance of 192 m and presents a curved alignment with a 312.5 m radius of curvature. According to AASHTO recommendations, the maximum superelevation rate of highway bridge decks corresponds to the minimum curve radius, as reported below [91]:

$$e_{\max} = 100\left(\frac{V^2}{127R_{\min}} - f_{\max}\right) \quad (1)$$

where $e_{\max}$ is the maximum superelevation rate, $f_{\max}$ is the maximum side friction coefficient ranging from 0.14 to 0.09 for highway bridges with design speeds (V) of 80~120 km/h [91]. Therefore, the design superelevation rate ranges from 1.5% to 6% to satisfy the curve radius requirements. To ensure driving comfort, a 1.5% superelevation is adopted, resulting in the asymmetrical design shown in Figure 1 (c). Such 1.5% super elevation can be interpreted as shifting the effective AOAs by about 0.86°. To study the asymmetrical effects of superelevation, the 0° wind yaw angle is set perpendicular to the girder axis, pointing uphill of the superelevation, while the 180° wind yaw angle is in the opposite direction. Figure 1 (d) presents the detailed diagrams of barriers, where the crash barrier (Type I) is 1.155 m high with a 42.5% porosity, and the median barrier (Type II) is 1.205m high with a 40% porosity.

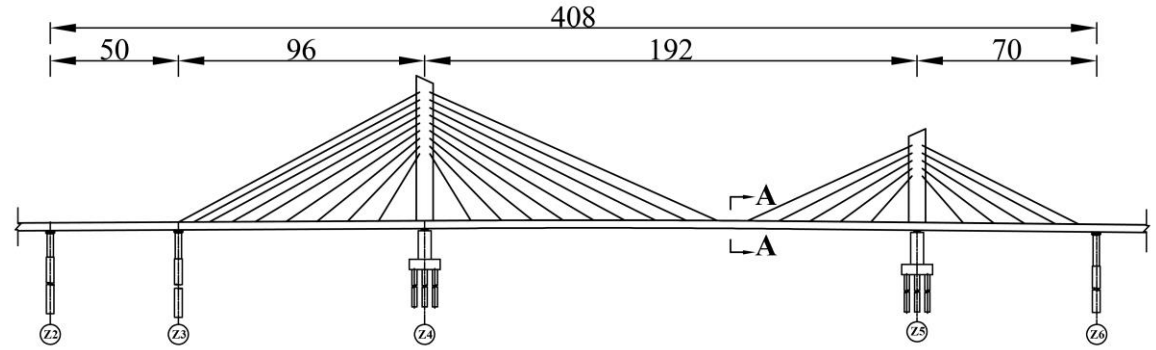

(a)

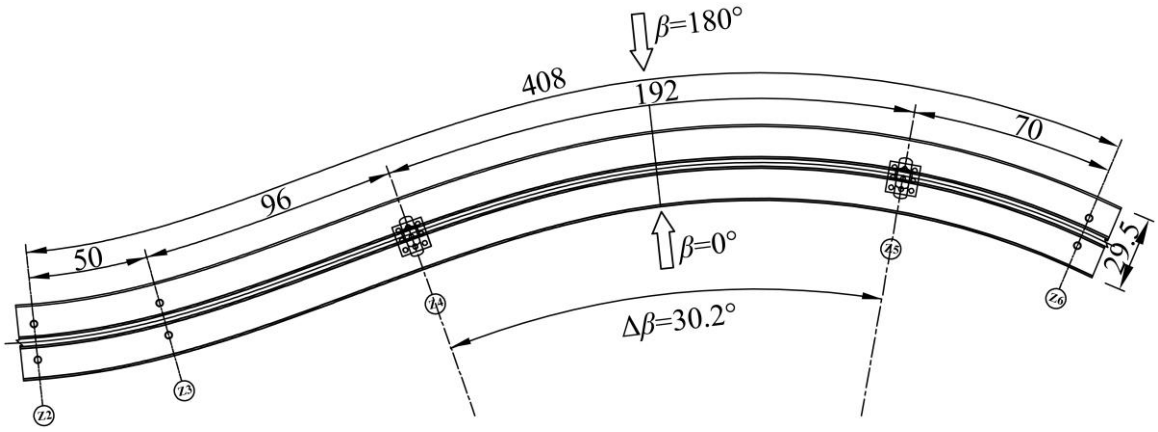

(b)

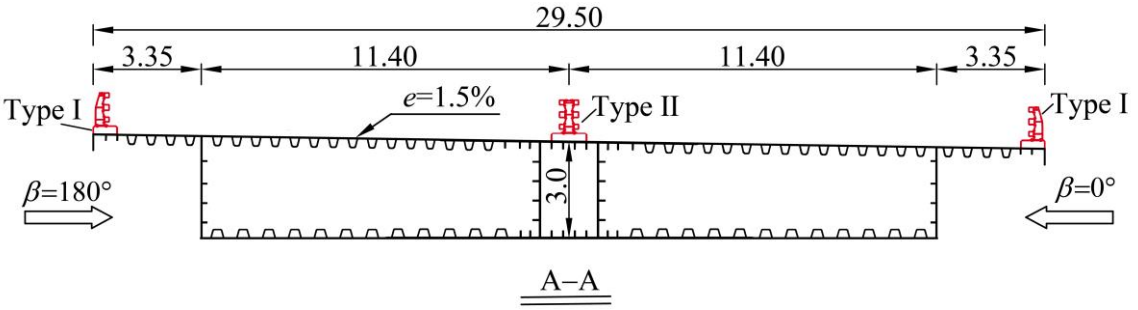

(c)

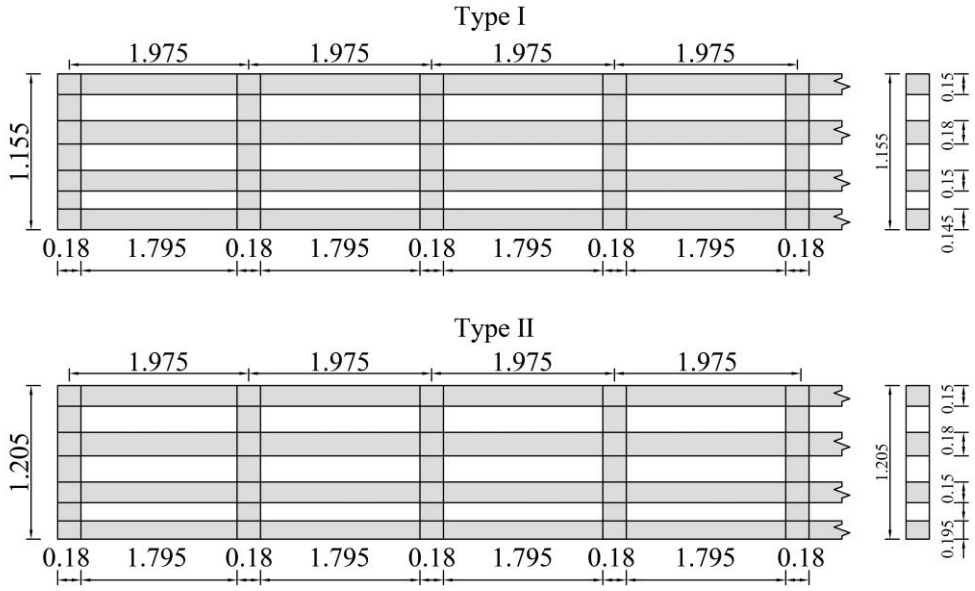

(d)

Figure 1. Schematic diagram of curved cable-stayed bridge (units: meters): (a) elevation view, (b) plan view, (c) steel box girder with a 1.5% superelevation, (d) details of barriers.

2.2 Sectional and full curved aeroelastic model

To investigate the effects of superelevation and spatial curves on VIVs, WTTs are conducted using both sectional and full aeroelastic models with the same geometric scale ratio of 1:50, minimizing potential discrepancies due to Reynolds number variations. In particular, the sectional WTTs model is tested in a smaller boundary layer wind tunnel with dimensions of 2.5 m (width) × 3.0 m (height) × 17.0 m (length) at Hunan University, China, while full model WTTs are performed in a larger wind tunnel with dimension of 12.0 m (width) × 3.5 m (height) × 18.0 m (length). All WTTs are conducted under smooth flow conditions with a free-stream turbulence intensity below 0.5%. The design parameters of the sectional and full model for vertical VIVs are detailed in Table 1, with maximum deviations within 7% of measured values.

Table 1 Design Parameters of the sectional and full bridge model

Parameters and symbols	units	Real bridge	Sectional model			Full model		
			Scale ratio	design value	Measured value	Scale ratio	design value	Measured value
Width B	m	29.5	1/50	0.59	0.59	1/50	0.59	0.59
Height D	m	3.0	1/50	0.06	0.06	1/50	0.06	0.06
Equivalent mass m_{eq}	kg/m	25258	$1/50^2$	10.10	10.10	-	-	-
Mass of main deck per length m	kg/m	19355	-	-	-	$1/50^2$	7.74	7.78
1st symmetric vertical frequency f_h	Hz	0.5922	7.59	4.492	4.492	$\sqrt{50}$	4.1875	3.906
1st symmetric torsional frequency f_t	Hz	1.7154	7.59	13.012	12.890	$\sqrt{50}$	12.13	12.21
Damping ratio ξ_h	%	-	1	-	0.35, 1.05	1	-	1.08

Figure 2 shows the free vibration system of section model WTTs. In particular, the sectional model has a width (B) of 0.59 m, a height (D) of 0.06 m and a span-length (L) of 1.54 m, with vertical blockage is less than 3% and length to height ratio of approximately 25.6. Two end plates are installed on both sides to ensure nominal two-dimensional flow [92, 93]. Two internal square steel framing systems are used to ensure overall rigidity of the model, while for the U ribs and diaphragms are 3D printed to accurately replicate the shape. The porous barriers are made of plastic materials (ABS), with the porosity calculated by the ratio of barriers voids and the entire frontal area [94, 95]. The damping ratios ξ_h of the vibration system are set to 0.35% and 1.05%, resulting in the Scruton number ($4\pi m_{eq}\xi_h/\rho BD$) of 10.2 and 30.6, respectively.

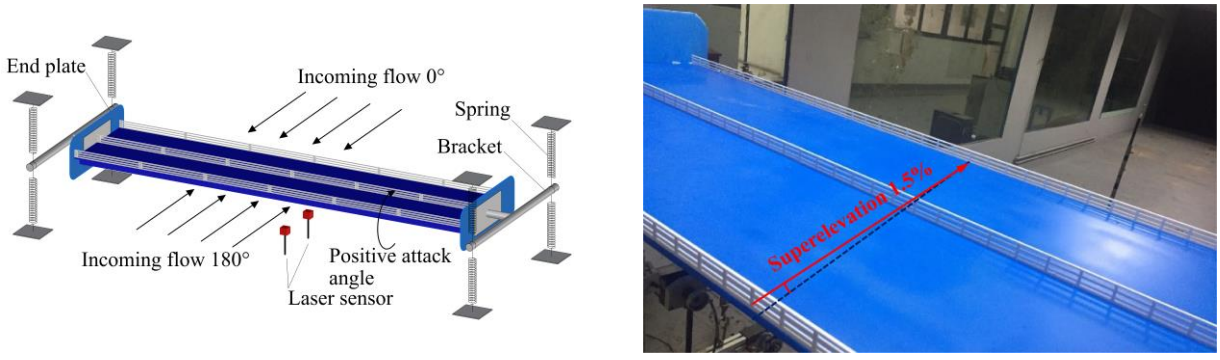

(a) (b)

Figure 2. Setup of Section model WTTs: (a) spring suspension system, (b) pictures.

Figure 3 shows the setup of full curved aeroelastic model WTTs (hereafter denoted as full model),

with design parameters determined using the similarity criteria and the optimization method proposed by Montoya et al. [96]. In particular, a curved aluminum alloy spine with a specially designed cross-section replicates the scaled lateral, vertical and lateral stiffness of the prototype bridge. To simulate the aerodynamic shape, 34 plastic cladding modules are spaced 2 mm apart, with additional iron mass blocks in each module to match the scaled mass and moment of inertia.

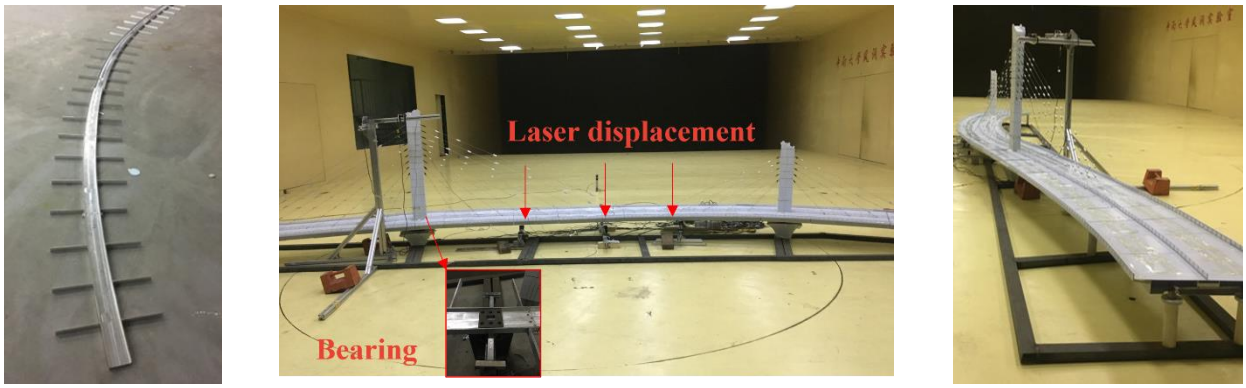

(a) (b) (c)

Figure 3. Full-bridge aeroelastic model in the wind tunnel: (a) curved spine, (b) elevation view, (c) side view.

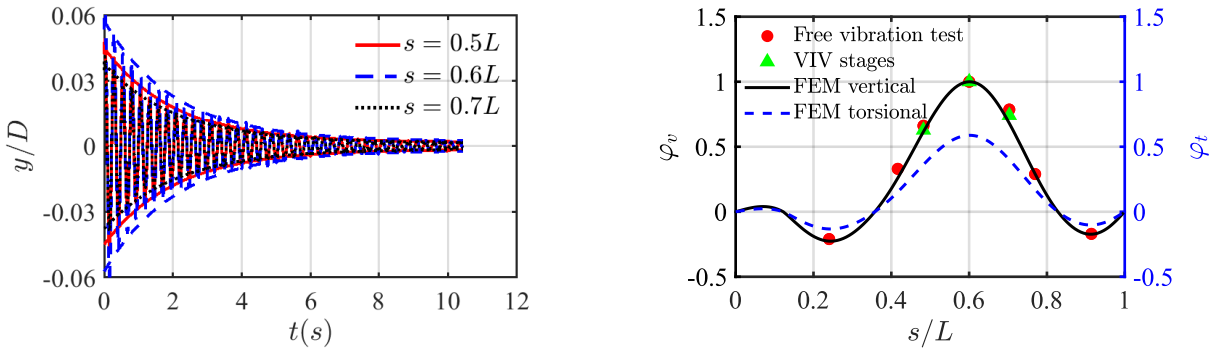

(a) (b)

Figure 4. Measured modal properties of full model: (a) damping ratio, (b) 1st coupled vertical-torsional mode shape.

According to the mode shape obtained by finite element analysis, six laser displacement sensors are positioned at the quarter-span (s=0.5L), mid-span (s=0.6L) and three-quarter span (s=0.7L) to capture the maximum VIV amplitude. Furthermore, four acceleration sensors are positioned at s=0.24L, 0.42L, 0.76L, and 0.91L to measure the mode shapes. Figure 4(a) shows the free decay curves of the full model at positions 0.5L, 0.6L and 0.7L, measured under artificial excitation with an amplitude approximating the maximum VIV amplitude of 0.06D. The damping ratio is determined by fitting the envelope curves at these three positions and averaging the results, yielding a value of 1.08%. This matches the values obtained for the sectional model, ensuring a consistent Scruton

number. Figure 4(b) compares the 1st symmetric vertical mode shape from free decay, VIV stages and finite element model (FEM) analysis, demonstrating good agreement between experiments and FEM results. Furthermore, significant coupled vertical bending-torsion vibrations are observed, with the ratio of torsional to vertical mode coordinates reaching approximately 0.59 at the maximum response (s=0.6L).

The wind speed varies from 0.3 to 14.0 m/s, corresponding to the deck width-based Reynolds number of 1.2×10^4 to 5.5×10^5. All tests focus on an AOA of +3° as the most significant VIV occurs, and at yaw angles of 0° and 180° to investigate asymmetric effects. Due to deck asymmetry caused by superelevation, section models are tested at 0° and 180° yaw angles, while the full model is tested at yaw angles from 0° to 180°.

3. Numerical settings

3.1 Computational domain and mesh

Figure 5 shows the computational domain used to simulate the CCB deck, which follows the Benchmark on the Aerodynamics of a Rectangular 5:1 Cylinder (BARC) [97] and previous FSI simulations [50, 51]. The computational domain size is 15B×98D, with a blockage ratio of 1.02%. To better control the mesh deformation and refinement in the region of interest, the domain is divided into three sub-regions, i.e., the inner rigid with the finest mesh ($4.0\times10^{-3}B$ in x-direction, $5.43\times10^{-4}B$ in y-direction), the deforming region with finer mesh ($8.4\times10^{-3}B$ in x and $7.34\times10^{-3}B$ in y) and the static region with a coarse mesh ($3.4\times10^{-2}B$). In particular, the rigid region moves together with the deck to ensure the near-wall mesh quality, capturing the important flow separation and reattachment. The deforming region uses a dynamic mesh to accommodate the displacement of inner rigid region, while the outer static region remains fixed. Furthermore, the 3D FSI meshes are generated by extruding the 2D mesh 1.5 B along the span-wise direction and subdividing into 41 layers [98, 99], resulting in a total of 5.89 million grid cells.

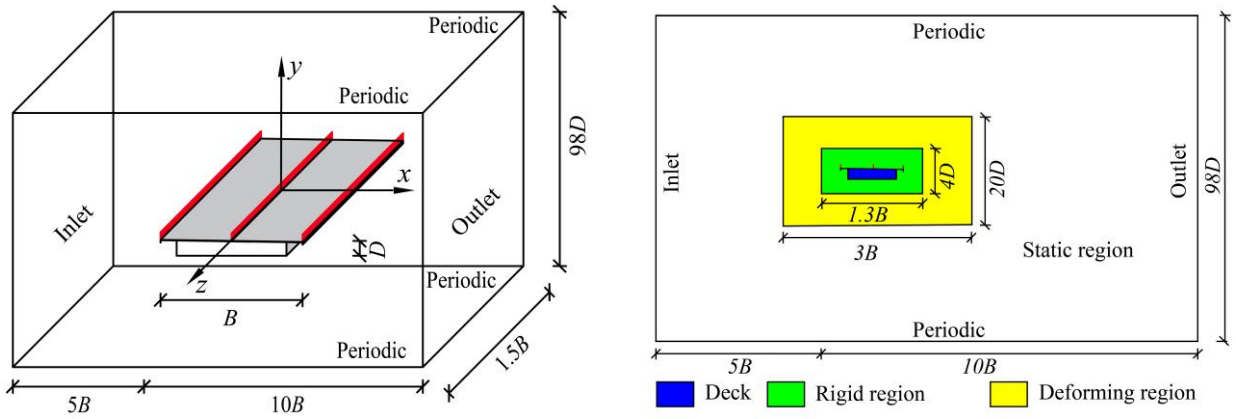

(a) (b)

Figure 5. Numerical model: (a) computational domain, (b) Mesh zones (not respect real proportions).

Figure 6 shows detailed meshes near the bridge deck and barriers. In particular, the meshes for superelevation rate of 1.5%, 4%, and 6% are adopted to study its effects on VIVs. Further, Figure 6(d) shows detailed meshes of the porous barriers generated using zero-thickness method proposed by the authors [90]. This approach employs the OpenFOAM CreateBaffles command to transform internal faces into boundary faces, forming a zero-volume porous baffle with a given shape. It ensures the porosity and barrier shape match the barriers adopted by the section model WTTs, while reducing excessive meshing and improving the efficiency of VIV simulations.

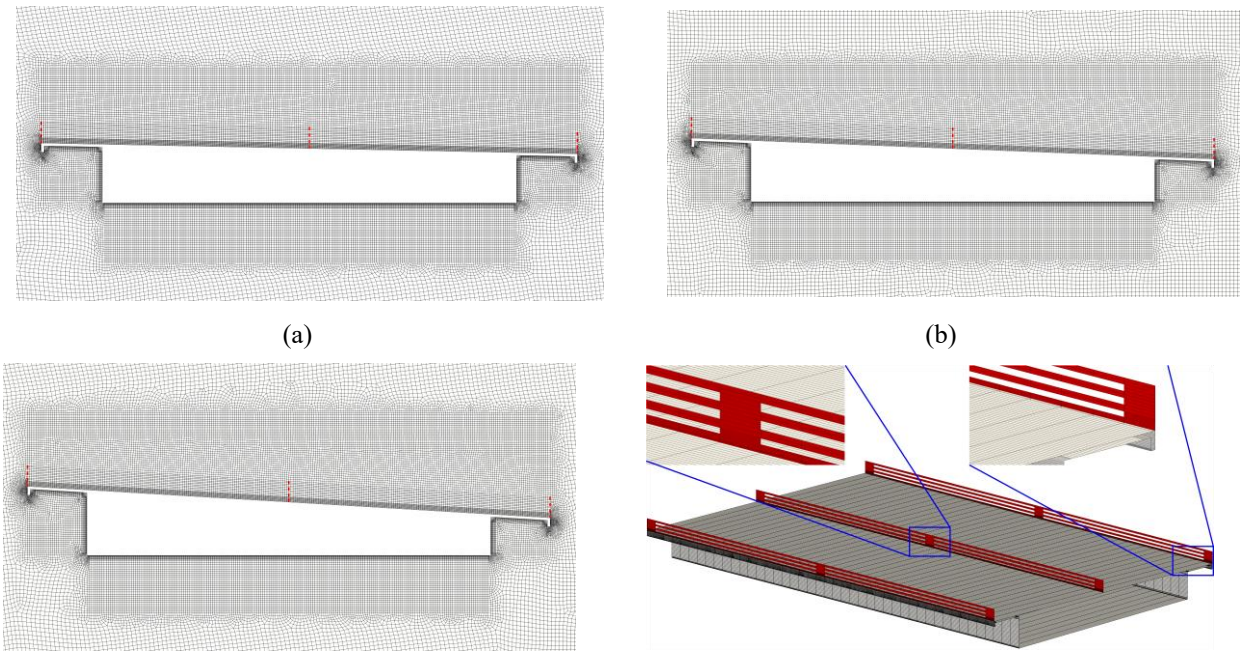

(a) (b)

(c) (d)

Figure 6. Numerical meshes near bridge deck using different superelevation: (a) e=1.5%, (b) e=4%, (c) e= 6%, (d) Zero-thickness barriers.

205 **3.2 Computational settings**

206 Regarding the turbulence model, 2D FSI simulations use the *k-ω* Shear Stress Transport (SST)
207 turbulence model [100] to solve the RANS equations, while 3D FSI simulation employs the *k-ω* SST
208 IDDES model [86, 87]. SST-IDDES applies the SST approach in the near-wall boundary layer and
209 uses a Large Eddy Simulation, LES, based sub-gird scale model in the free shear region, taking
210 advantage of LES's accuracy and RANS's efficiency.

211 Regarding the numerical schemes, the time integration is performed using a second-order Crank-
212 Nicolson scheme with an implicitness factor of 0.9. The advective terms are approximated using the
213 Linear Upwind Stabilized Transport (LUST) scheme, while pressure-velocity coupling is solved
214 using the PIMPLE algorithm [101]. Regarding the boundary conditions, at the inlet a Dirichlet
215 condition is imposed on the turbulent kinetic energy, k, and the specific dissipation rate, ω, while a
216 Neumann condition is applied to pressure. The values of k and ω is calculated as [102]:

217 $$k = \frac{3}{2}(UI)^2, \quad \omega = \frac{k^{0.5}}{C_\mu^{0.25} l} \tag{2}$$

218 where U is the freestream velocity, I is the turbulence intensity (set to 0.5%), l is the characteristic
219 eddy length scale (set to 0.03 m) and $C\mu$ = 0.09. Wall-functions are applied to the bridge deck and
220 barriers, and periodic conditions are applied to the top, bottom, and side surfaces. Dynamic
221 simulations are conducted using the *sixDoFRigidMotion* dynamic mesh solver. The morphing mesh
222 is updated using the Symplectic methods [103, 104] to solve the motion differential equation which
223 can be expressed as follows:

224 $$m\ddot{y}(t) + 4\pi\xi_h f_h \dot{y}(t) + 4\pi^2 f_h^2 m y(t) = \frac{\rho U^2 B}{2} \int_z C_L(t) R(z) dz \tag{3}$$

225 where y denotes the displacement, and the dot symbol represents a time derivative. In accordance
226 with WTTs, the modal mass per unit length m is 9.805 kg/m, and the modal frequency f_h is 4.492 Hz.
227 ρ is the air density, while $C_L(t)$ and $R(z)$ are the lift coefficients and spanwise correlations.

228 Table 2 summarizes the numerical setups used to study VIVs of the CCB deck. In Setup 1, 2D
229 URANS simulations compare yaw angles of 0° and 180° to study the asymmetry effects. In Setup 2,
230 3D IDDES is used to simulate the maximum VIV case at a 180° wind yaw angle, allowing a
231 comparison of 2D and 3D FSI simulation accuracy. In Setup 3, both 2D URANS and 3D IDDES

investigate the effects of superelevation by varying it from 4% to 6%. For 2D URANS, the reduced wind speeds (U/f_hB) range from 0.36 to 3, consistent with those in the WTTs, while 3D IDDES focuses on a range of 1.34 to 2.88, capturing only the second lock-in region where maximum VIVs occurs.

Table 2 Numerical setups for obtaining VIVs of CCB deck

Case	Methods	wind yaw angles	superelevation (e)	Reduced wind speeds(U/f_hB)
Setup 1	2D URANS	0°, 180°	1.5%	0.36~3.00
Setup 2	3D IDDES	180°	1.5%	1.34~2.88
Setup 3	2D URANS, 3D IDDES	180°	4%, 6%	0.36~3.00, 1.34~2.88

All Reynolds number are consistent with WTTs, and the maximum Courant number remain below 1.25 for URANS and 1.73 for IDDES, occurring only in a few small cells. Simulations are performed using OpenFOAM-v2112 and covers 90 stable VIV periods. Due to high computational demands of FSI simulations, 2D URANS case used 24 cores on a workstation and 3D IDDES used 128 cores on the National Supercomputer Center in Tianjin.

3.3 Preliminary checks

Table 3 details the properties used for the mesh independence study. Three different meshes using zero-thickness barrier, denoted as *Coarse*, *Medium*, and *Fine*, are used to assess mesh independence of the results. The size of the finest rigid mesh near the deck, $\Delta x/B$, decreases from 5.96×10^{-3} to 3.0×10^{-3}, while the first layer height, $\Delta h/B$, decreases from 8.63×10^{-4} to 3.64×10^{-4}. The number of boundary layers n_{BL} increase from 24 to 49, resulting in a total number of mesh ranges from 84.6k to 195.6k. The Maximum Courant number ranges from 0.79 to 1.88 and corresponding computational time for 10 stable VIV cycles is about 13.6 to 31.5 core hours. Furthermore, a modified *Medium* mesh with full-thickness barriers is generated to compare the accuracy of the zero-thickness barrier approach. Detailed mesh near the deck and barriers are shown in Figure 7.

Table 3 Mesh properties of main girder with different mesh

Barrier Method	Mesh	$\Delta x/B$	$\Delta h/B$	n_{BL}	Total cells (k)	$U\Delta t/B$	Maximum Courant number	Core hours per 10 VIVs
Zero-thickness	*Coarse*	5.96×10^{-3}	8.63×10^{-4}	24	84.6	7.15e-4	0.79	13.6
	Medium	4.0×10^{-3}	5.43×10^{-4}	35	143.9	7.15e-4	1.25	24.7
	Fine	3.0×10^{-3}	3.64×10^{-4}	49	195.6	7.15e-4	1.88	31.5
Full-thickness	*Medium*	4.0×10^{-3}	5.43×10^{-4}	35	155.8	7.15e-5	1.46	171.3

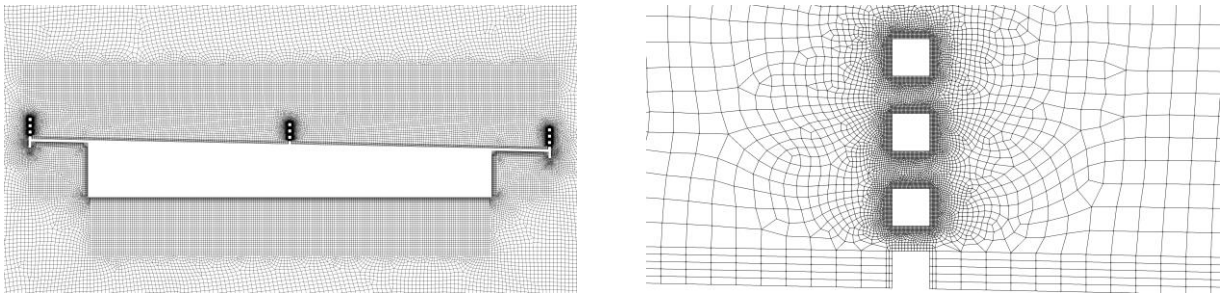

(a) (b)

Figure 7. Mesh using the traditional full-thickness methods near: (a) CCB deck, (b) barriers.

Figure 8 provides 2D URANS results for pressure distributions at reduced speeds $U/(f_hB)$ of 1.613 using three different meshes. The results are consistent across the meshes, except for minor differences in the standard deviation near the trailing edge of the upper surface.

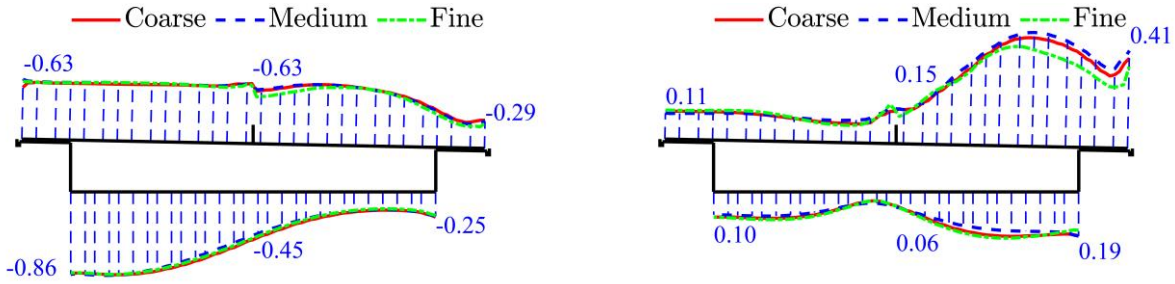

(a) (b)

Figure 8. Pressure coefficient distribution of the bridge deck at VIVs onset reduced speeds $U/(f_hB)$=1.613: (a) time-averaged, (b) standard deviation.

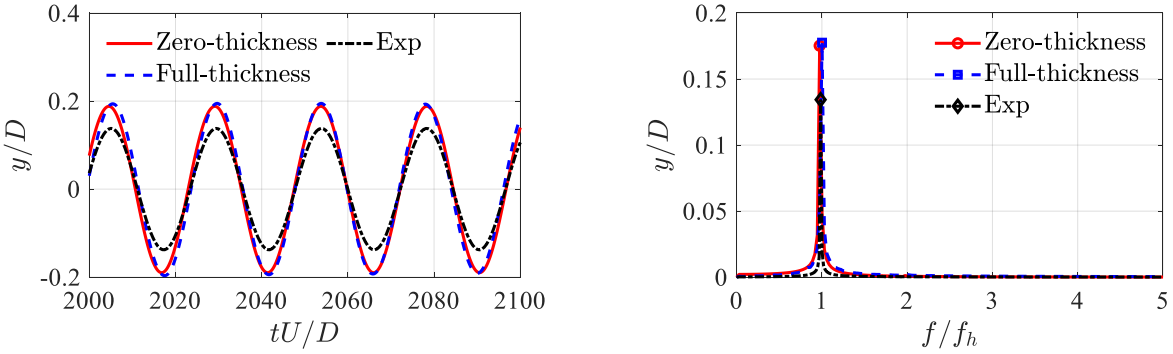

(a) (b)

Figure 9. VIV displacements at maximum VIV position obtained by 2D URANS: (a) time history, (b) FFT.

Figure 9 compares the VIV displacements at the maximum VIV position using zero-thickness and full-thickness barriers obtained by 2D URANS. The results show that both methods yield nearly identical VIV responses and exceeds WTTs results. Notably, with comparable Courant number, the computational time for 10 VIV cycles is 24.7 core hours for zero-thickness barriers and 171.3 core

hours for full-thickness barriers. This indicates using zero-thickness barriers speeds up the FSI simulations by 6.9 times without losing accuracy. Therefore, the medium mesh using zero-thickness barriers is chosen for the following simulations to balance efficiency and accuracy.

4. Results and discussions

This section presents VIV results for the CCB deck under opposite inflow directions and varying superelevation. In particular, Section 4.1 compares VIVs from sectional model WTTs and CFD simulations, while Section 4.2 provides the corresponding pressure distributions and flow fields. Finally, Section 4.3 examine the effects of spatial curvature by comparing the section and full model.

4.1 Effects of superelevation on VIVs

To examine the superelevation-induced asymmetry effects, Figure 10 and Figure 11 present a comparison of vertical VIV responses obtained from WTTs, 2D URANS and 3D IDDES at wind yaw angles of 0° and 180°, respectively. The limit values, specified by the Wind-Resistant of Chinese Highway Bridge Code [105], are calculated as follows:

$$[Y]/D=[0.04/f_h]/D=0.0675/3=0.0225 \tag{4}$$

The figures show that the CCB deck exhibits significant vertical VIVs in two distinct lock-in regions at both 0° and 180° yaw angles, with amplitudes far exceeding the limit value. For WTTs at 0° yaw angle, the first lock-in region occurs at reduced speeds of approximately 0.847~1.124 and the second at 1.676~2.320, with maximum amplitudes reaching 0.04D. The VIV onset reduced speeds are consistent with the empirical formula proposed by Shiraishi and Matsumoto [106]:

For the first vertical VIV: $V_{cr1}=(1/n)\times 1.67\times(B/D)\times(D/B)=1/2\times 1.67=0.835$.

For the second vertical VIV: $V_{cr2}=(1/n)\times 1.67\times(B/D)\times(D/B)=1/1\times 1.67=1.67$.

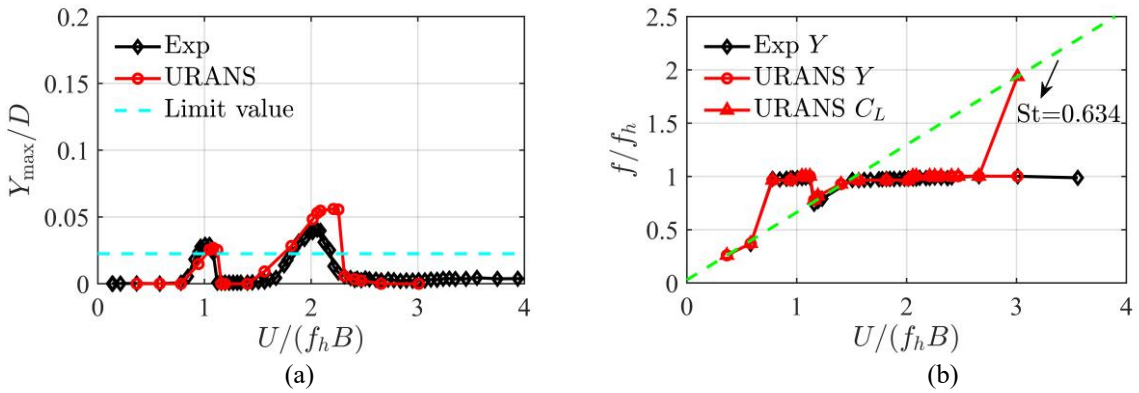

(a) (b)

Figure 10. VIV responses for 0° yaw angle: (a) amplitude, (b) frequency.

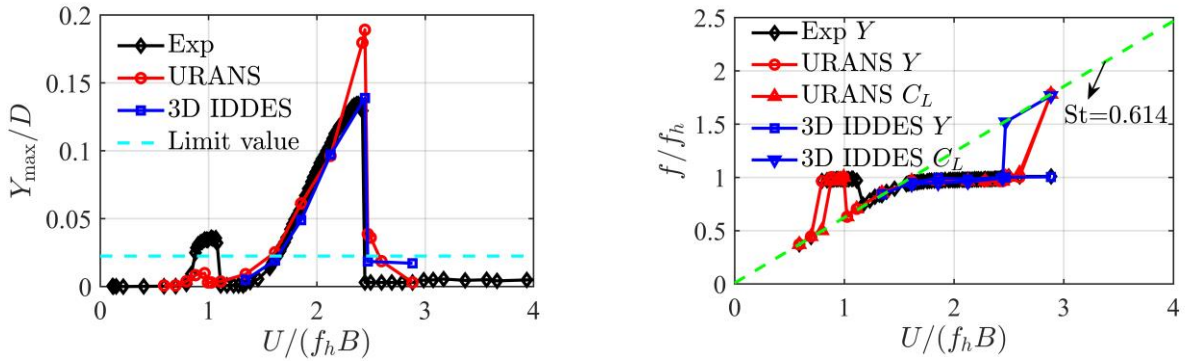

(a) (b)

Figure 11. VIV responses for 180° yaw angle: (a) amplitude, (b) frequency.

For WTTs at opposite 180° yaw angle shown in Figure 11, the first and second lock-in regions extend to approximately 0.84~1.12 and 1.57~2.45, respectively. The maximum VIV amplitude reaches 0.134*D*, approximately 3.35 times higher than that of 0° yaw angle. Figure 10(b) and Figure 11(b) show that frequencies of VIV displacements and forces are locked to the section model frequency, corresponding to Strouhal numbers of 0.634 and 0.614, respectively. This indicates that a 1.5% superelevation has a slight effect on the Strouhal number but significantly increase VIV amplitudes when inflow direction is reversed. Hence, the adverse asymmetric effects of superelevation on VIVs must be considered in the design of CCBs.

Compared to WTTs, the present FSI simulations can well reproduce the VIV lock-in regions and frequencies. However, 2D URANS underestimate VIV amplitudes in the first lock-in region and overestimates them in the second, while 3D IDDES provides more accurate predictions. Figure 12 compares the time history and FFT curves of VIV displacements at the maximum VIV position in the second lock-in region. The figure shows that 2D URANS overestimates the VIV amplitude by approximately 35.0% at 0°and 31.6% for 180° angle, while IDDES closely matches WTTs with only 3.3% deviation. Figure 13 further compares the corresponding lift coefficients at the maximum VIV position. At a 180° yaw angle, both 2D URANS and 3D IDDES predict significantly higher lift coefficients than at 0°, leading to a larger VIV response. Furthermore, URANS 180° predicts a higher lift coefficient than 3D IDDES, exaggerating the VIV response. Notably, all lift coefficients show super-harmonics components, which may result in the presence of two lock-in regions [107].

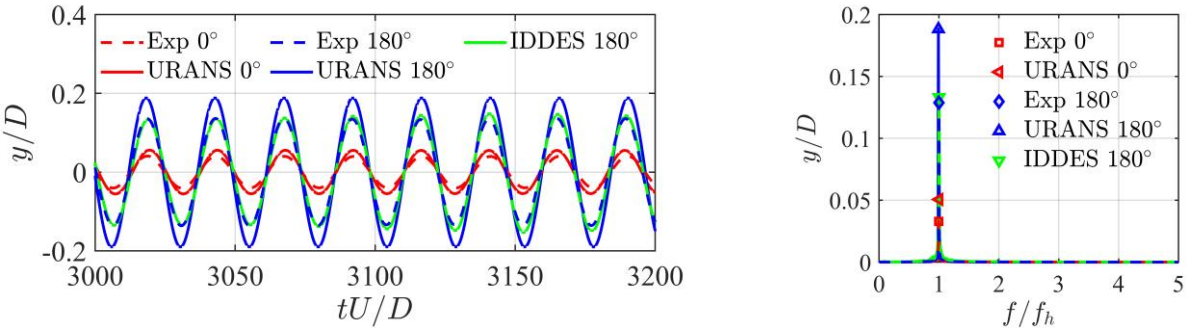

(a) (b)

305 Figure 12. VIV displacements at maximum VIV position: (a) time history, (b) FFT.

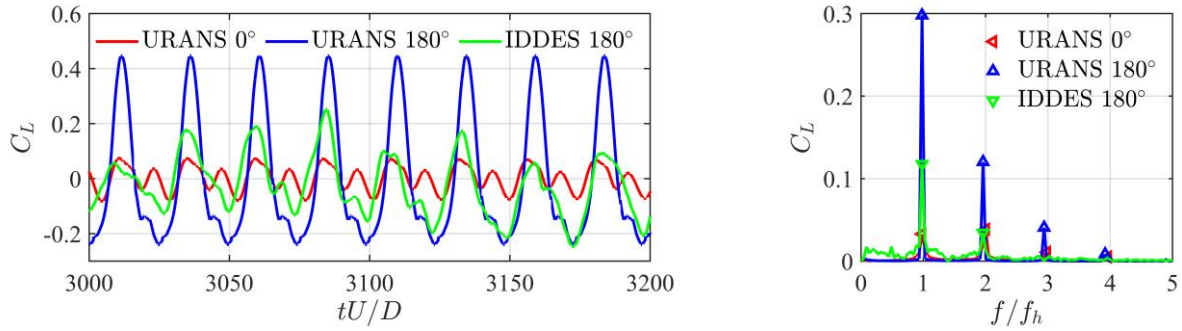

(a) (b)

306 Figure 13. Lift coefficient at maximum VIV position: (a) time history, (b) FFT.

307 To study the effects of the superelevation rate, Figure 14 presents URANS results for VIVs and
308 the frequency ratio (f/f_h) of CCB deck with different superelevation at a 0°yaw angle. As the
309 superelevation rate increases from 1.5% to 6%, the maximum VIV amplitude in the first lock-in
310 region decreases about 32.25%, while the second lock-in region nearly disappears. Figure 14(b)
311 shows that higher superelevation increases the Strouhal number from 0.634 at 1.5% to 1.18 at 6%,
312 causing the second lock-in region to vanish.

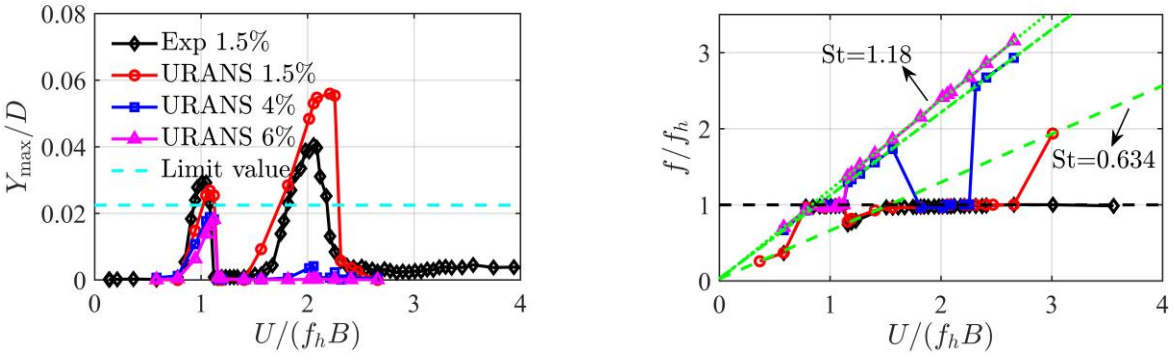

(a) (b)

313 Figure 14. VIVs of different superelevation at 0° yaw angle: (a) amplitude, (b) frequency (f from C_L for URANS).

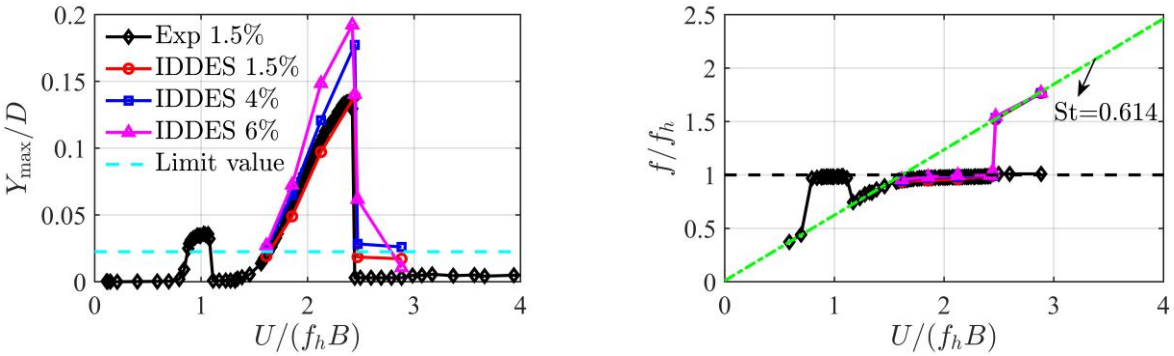

(a) (b)

Figure 15. VIVs of different superelevation at 180° yaw angle: (a) amplitude, (b) frequency (f from C_L for IDDES).

Given the high accuracy of 3D IDDES for the CCB deck at 180° yaw angle, Figure 15 shows the obtained VIV responses for different superelevation. Contrary to the trend observed at 0°, as superelevation increases from 1.5% to 6%, the maximum VIV amplitude at the second lock-in regions rises by approximately 38%, with the Strouhal number stays nearly the same.

4.2 Pressure distributions and flow fields

Next the pressure distributions are analyzed to clarify the superelevation effects and highlight discrepancies between 2D URANS and 3D IDDES. Figure 16 presents pressure distributions at the maximum VIV position for wind yaw angles of 0° and 180°. It shows that both mean and fluctuating pressures at 180° are higher than those at 0°, with a sharp drop at the median barrier, followed by a sudden increase in fluctuating pressure in its wake region. Compared to 3D IDDES, URANS 180° predicts higher fluctuating pressures on the upper surface and a downstream shift in the vortex reattachment point, with the maximum standard deviation points at x=0.26B for URANS and 0.2B for IDDES. Further, URANS 180° underestimates fluctuating pressures on the lower surface, indicating it may not accurately capture flow separation in this region. Further analysis (not included for brevity) confirms that mesh refinement does not affect URANS results.

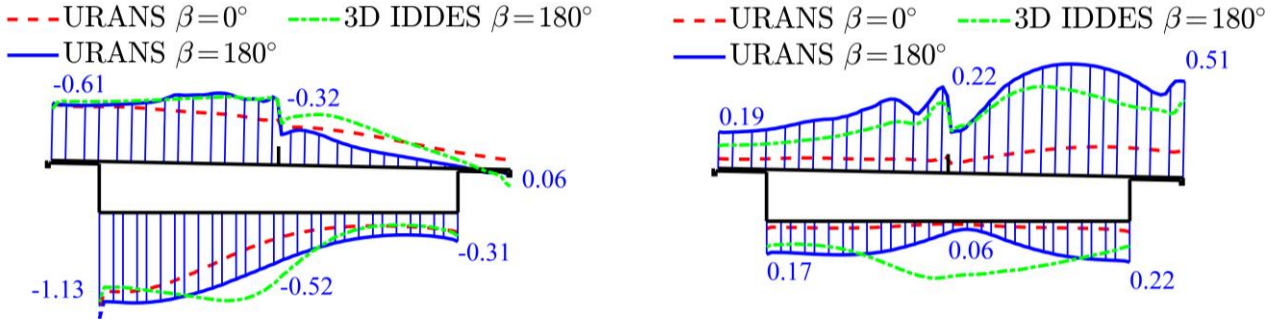

(a) (b)

Figure 16. Pressure coefficients distribution at maximum VIV position: (a) mean, (b) standard deviation.

Figure 17 compares the corresponding time-averaged streamlines and at the maximum VIV positions for URANS 0°, URANS 180° and 3D IDDES 180°. On the upper surface, flow separation at the windward barrier forms the main vortex region $U1$, covering the front half of the deck. Then, vortex $U1$ interacts with the median barrier forms secondary vortices region ($U2$). Compared to 0°, superelevation of 180° yaw angle increases the angle between inflow and the upper surface, leading to higher vortex curvature. On the lower surface, flow separation at the leading edge forms the vortices $L1$. Notable, the vortex cores are remarkably different between URANS and IDDES. In 3D IDDES the vortices have an elongated drop shape and longer reattachment length while in 2D URANS they appear more elliptical. This difference is due to URANS inability to capture the inner region near the leading edge, which have been discussed by Bruno et al. [108] and Patruno et al. [109] in the stationary case of a 5:1 rectangular cylinder.

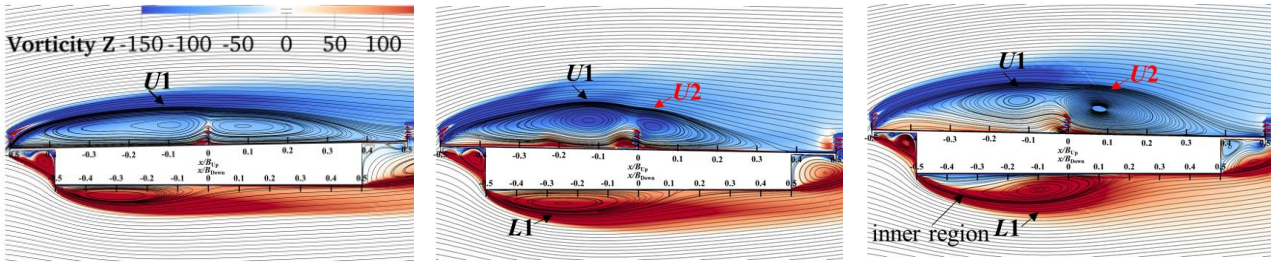

(a) (b) (c)

Figure 17. Time-averaged streamlines colored by vorticity at maximum VIV: (a) URANS 0°, (b) URANS 180°, (c) IDDES 180°.

To clarify flow fields responsible for differences in VIV responses, Streaming Total Dynamic Mode Decomposition (STDMD) [110, 111] are applied to the vorticity fields. In particular, A total of 1300 snapshots with a time interval of 0.007s are recorded, covering about 40 vortex shedding periods. Figure 18 shows the eigenvalues of the first six models and their corresponding modal energy obtained from 2D URANS at the maximum VIV positions. The eigenvalues lie close to the unit circle, indicating that the associated flow structures are periodically stable with time. Furthermore, the zero model (f/f_h=0) represents the time-averaged flow fields and accounts for approximately 99.1% of the total energy, which is consistent with the findings by [112]. The frequencies of following model are 1~5 times the natural frequency of the CCB deck (f_h). Among them, the first model (f/f_h=1) that governs the VIV response has significantly higher energy than the following modes, while the cumulative modal energy reaches 99.7% by the first three mode that govern the flow dynamics.

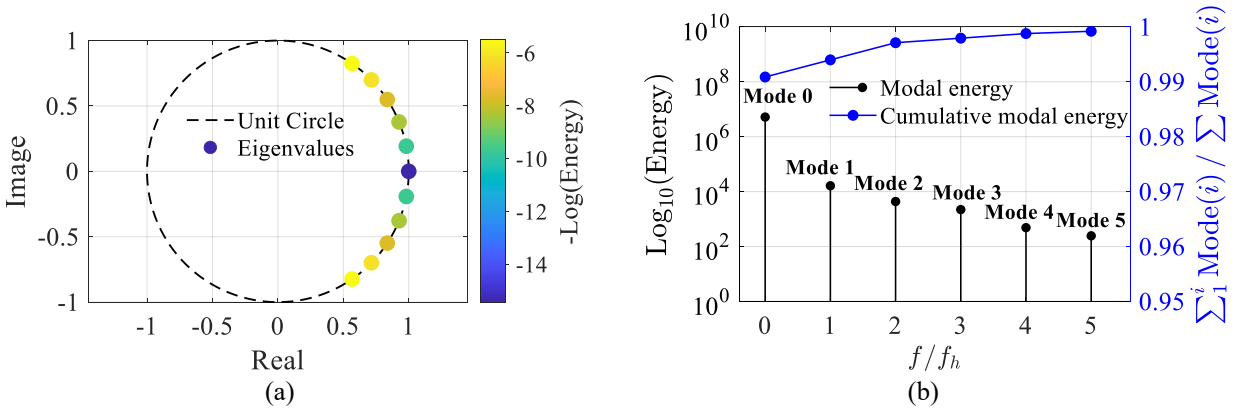

Figure 18. STDMD of vorticity at maximum VIV position obtained by URANS 180°: (a) eigenvalues, (b) modal energy.

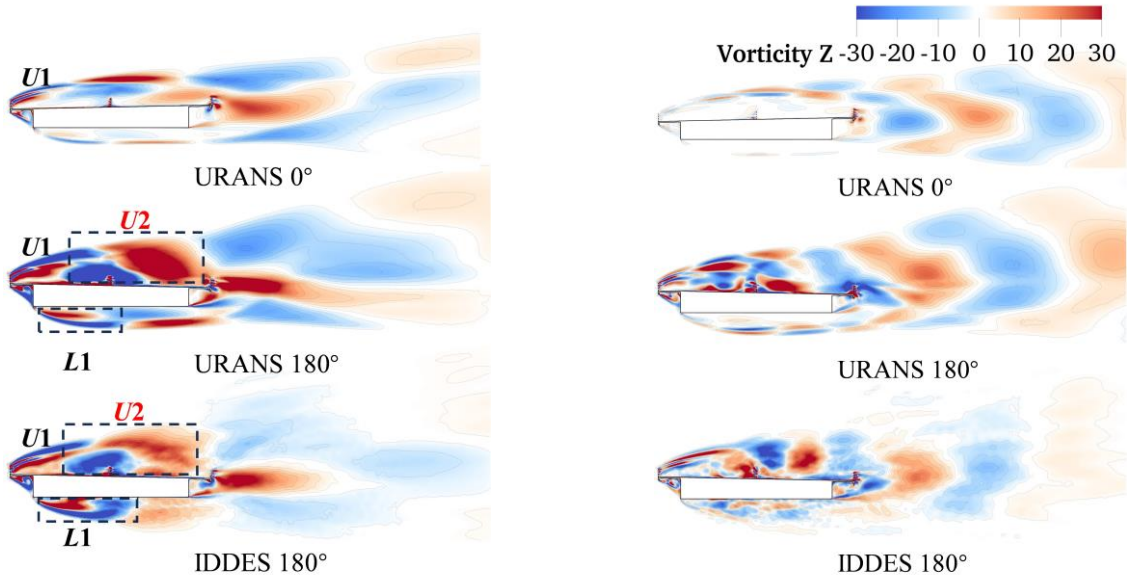

Figure 19. STDMD models of vorticity at maximum VIV position: (a) first model (f/f_h=1), (b) second model (f/f_h=2).

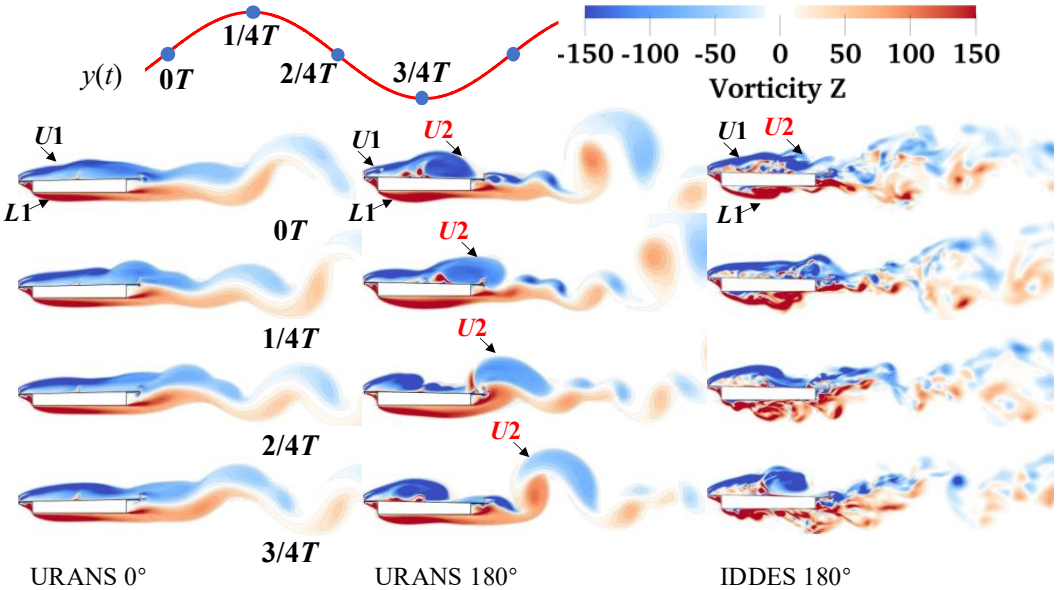

Figure 20. Vorticity evolution diagram during vibration period T at maximum VIV positions.

Figure 19 compares the first model (f/f_h=1) and second model (f/f_h=2) using STDMD from URANS 0°, URANS 180° and IDDES 180°. Figure 20 further shows the vorticity distributions during one vibration cycle. It shows that in URANS 0°, the main vortices $U1$ and $L1$, forming on the upper and lower surfaces of the deck, eventually develop into a Kármán vortex street in the tail of bridge deck. In contrast, in URANS 180°, separated vortices not only form on the windward barrier $U1$, but also as strong secondary vortices $U2$ downstream of the medium barrier, leading to stronger and higher Kármán vortex street in the tail region. The first mode of the STDMD shows that these secondary vortices $U2$ are fed by the counter-rotating vortex in adherence to the medium barrier, driven by the shielding effect of superelevation. Compared to IDDES 180°, URANS 180° produces a similar separation bubble ($U1$ and $U2$) on the upper surface. Nevertheless, IDDES exhibits small and irregular vortices, while URANS shows more stable vortices and smooth shear layer thickening. For the lower surface, IDDES can reproduces inner recirculation regions compared to URANS, leading to a stronger main vortex ($L1$) with higher vorticity and larger vortex-induced forces.

Next the influence mechanisms of the superelevation rates on VIVs are presented. Figure 21 presents pressure distributions from URANS at 0° for various superelevation rates. As the superelevation increases, the mean pressure coefficients gradually decrease, while the standard deviation drops sharply, causing the vanish of the second VIV region at 0°. In contrast, Figure 22 further presents pressure coefficient distributions in the middle position from IDDES at 180° yaw angle. Compared to 0°, the fluctuating pressure is significantly higher, resulting in a larger VIV response. As superelevation increases, both the mean and standard deviation exhibit slightly variations around the wake region of the medium barrier.

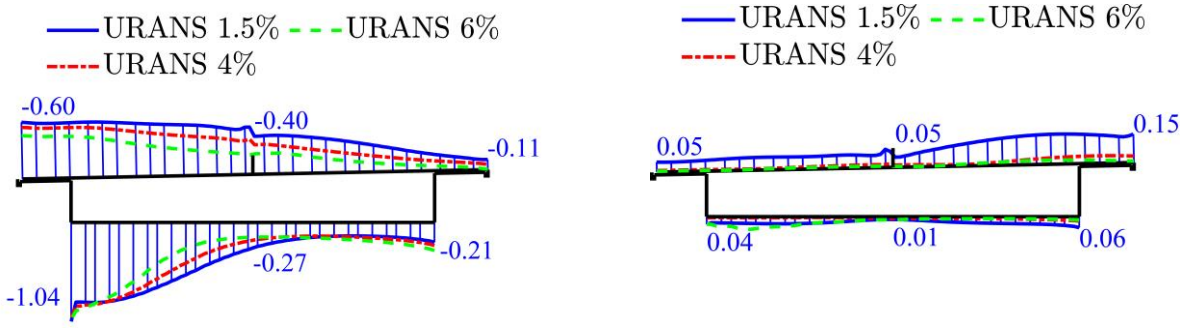

(a) (b)

Figure 21. Pressure coefficient at maximum VIV amplitude in the second lock-in region for 0° yaw angles: (a) mean, (b) standard deviation.

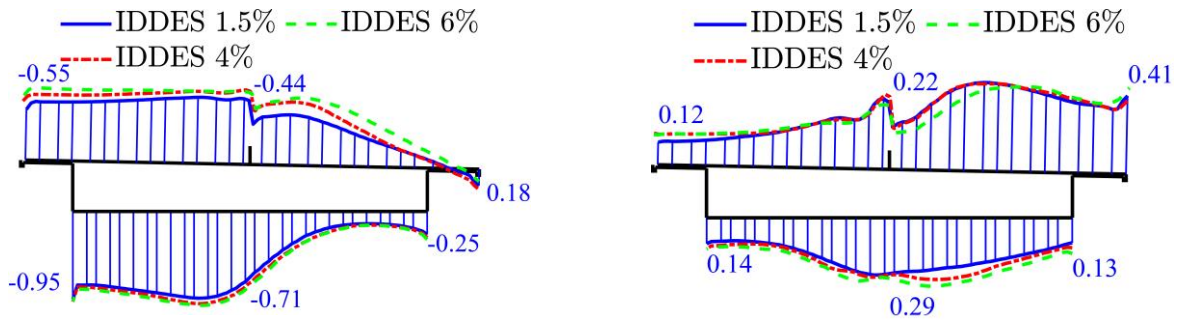

(a) (b)

Figure 22. Pressure coefficient at maximum VIV position for 180° yaw angles: (a) mean, (b) standard deviation.

Figure 23 and Figure 24 further respectively show the instantaneous *Q*-criterion flow fields at peak VIV and the STDMD models for different superelevation rate. It shows that increasing superelevation affects the separated shear layers and flow structures around the medium barrier, leading to a further increase in the amplitudes of VIV.

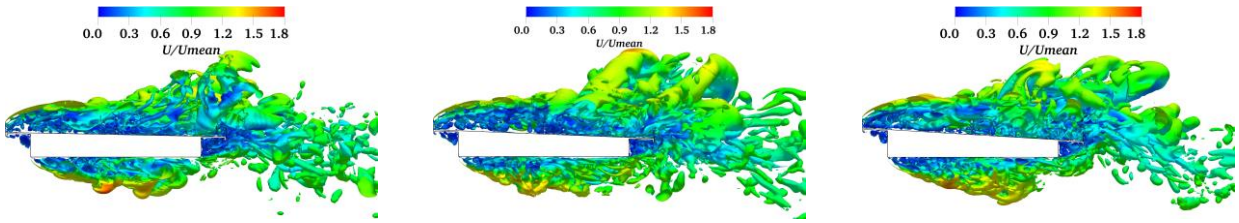

(a) (b) (c)

Figure 23. Instantaneous *Q*-criterion flow fields at the time of maximum vertical displacement for different superelevation: (a) *e*=1.5%, (b) *e*=4%, (c) *e*=6%.

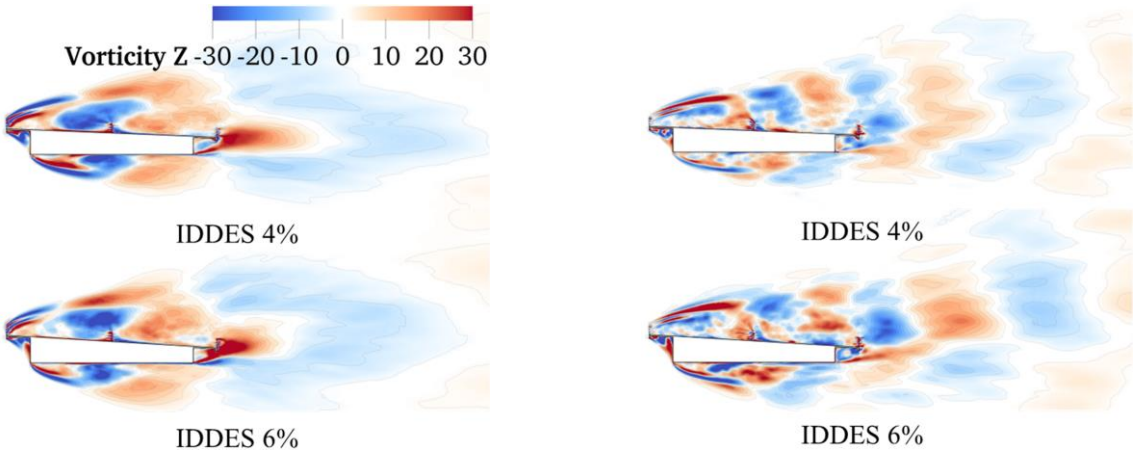

(a) (b)

Figure 24. STDMD models of vorticity at maximum VIV position: (a) first model (f/f_h=1), (b) second model (f/f_h=2).

Finally, to clarify the span-wise effects for calculating the subsequent MSCF of the CCB, Figure 25 presents the spanwise correlation of four pressure taps (x/B_{Up}, x/B_{Down}=±0.4，±0.2) and the overall VIV forces obtained by 3D IDDES. Notably, the overall lift coefficient correlation exceeds 0.8,

closely matching the WTTs of a box girder with barriers by Sun et al. [113]. The adopted fitting curves follow the exponential law proposed by Ricciardelli [114] as follows:

$$R(\Delta z / D) = (1-d)\exp[-c(\Delta z / D)] + d \tag{5}$$

where c=0.9591 denotes the decay coefficient, and d=0.8469 indicates the horizontal asymptote. Compared to 2D URANS, 3D IDDES can account the imperfect spanwise correlations, yielding VIV amplitudes closer to WTTs results.

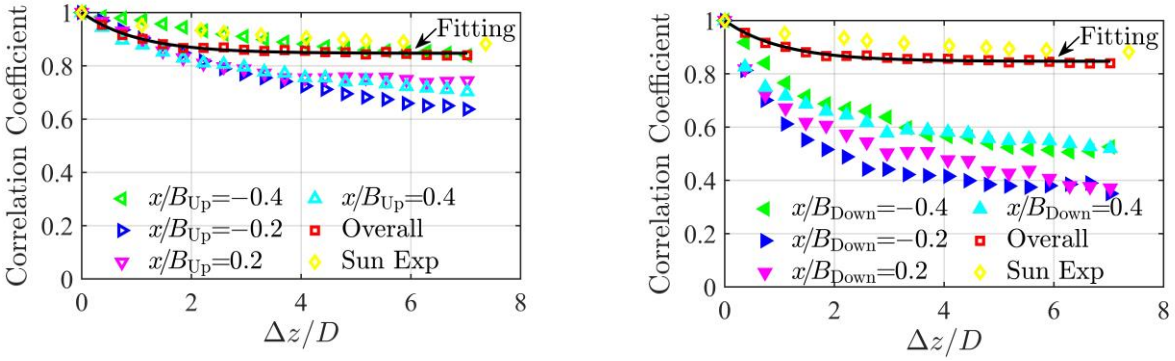

(a) (b)

Figure 25. Span-wise correlations at maximum VIVs for 180° yaw angle: (a) upper surface, (b) lower surface.

4.3 Effects of spatial curvature and MSCF by comparing sectional and full model

Figure 26 presents the vertical and torsional VIVs measured at the maximal point (s=0.6L) for yaw angles of 0°, 30°, 60°, 150°, and 180°. Both the vertical and torsional VIV amplitudes decrease sharply as the yaw angle increases, consistent with Wang et al.'s [75] findings on VIVs of rectangular cylinder in skew winds. In particular, the vertical VIV amplitudes at 0° and 180° are 0.014D and 0.061D, respectively, indicating that the superelevation increases VIV amplitude by about 4.36 times between opposite wind directions. This increase exceeds that in the section model, likely due to the differing effects of spatial curvature at 0° and 180° (see in Figure 1 (b)). Furthermore, Figure 27 shows the time history and FFT curves of coupled vertical-torsional VIVs measured at the maximum VIVs position of full model. The coupled VIVs occur at the same frequency and the torsional to vertical VIV ratio is approximately 0.59, which matches the mode ratio of the CCB (see Figure 4(b)).

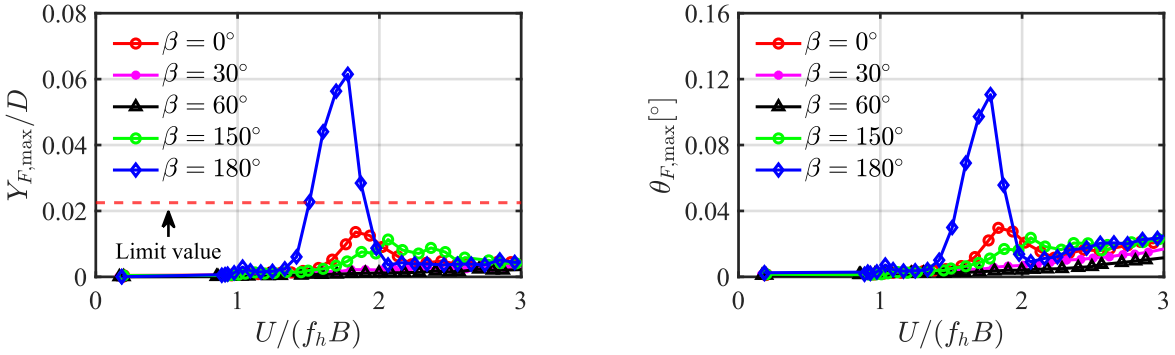

(a) (b)

412 Figure 26. VIV amplitudes obtained from full model WTTs at different wind yaw angles: (a) vertical response, (b)

413 torsional response.

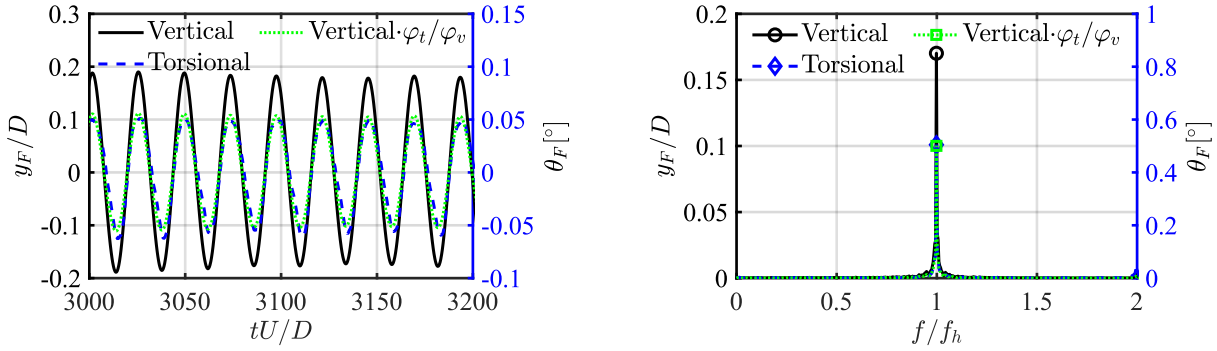

(a) (b)

414 Figure 27. Coupled vertical-torsional VIVs displacement of the full model measured at the maximum VIVs position: (a)

415 time history, (b) FFT.

416 In order to clarify the effects of span-wise curvature, Figure 28(a) compares vertical VIV

417 responses from straight section and curved full model WTTs at a 180° yaw angle. To ensure the same

418 Scruton and Reynolds numbers, section model VIVs with a closely matched damping ratio of 1.05%

419 were selected. It can be found that vertical maximum VIVs occurs at a reduced speed of 2.04 for

420 section model and 1.78 for full model, with the corresponding maximum amplitudes of 0.0481D and

421 0.0614D, respectively. This indicates that spatial curvature leads to an earlier onset of maximum VIV

422 by approximately 0.264 in reduced speeds, equivalent to a real wind speed difference of 4.61 m/s.

423 The experimental MSCF is calculated by the ratio of the maximum vertical VIV amplitude between

424 the sectional and full model, yielding a value of 1.28.

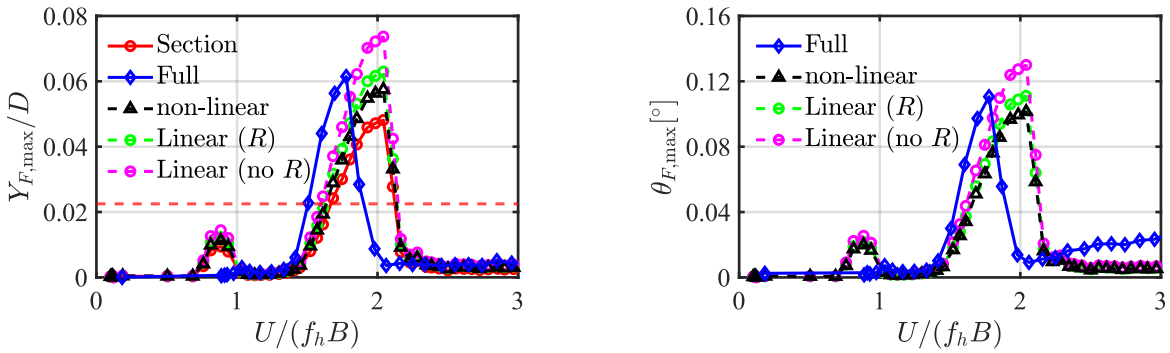

Figure 28. VIV amplitudes between the section and the full model with nearly identical damping ratios and Sc numbers at a 180° yaw angle: (a) vertical response, (b) torsional response.

Assuming the same Strouhal and Scruton numbers, the theoretical MSCF of CCBs can be obtained according to Scanlan's linear and nonlinear models[34, 83]:

$$\gamma_{\text{linear}} = \frac{Y_F}{Y_s} = \frac{\int_L |\varphi_v(s)| R(s) ds}{\int_L \varphi_v^2(s) ds},\ \gamma_{\text{non-linear}} = \sqrt{\frac{\int_L \varphi_v^2(s) ds}{\int_L \varphi_v^4(s) ds}} \tag{6}$$

Where $\varphi_v(s)$ is the first vertical bending mode shape that shown in Figure 4(b), $R(s)$ is the span-wise correlation factor of VIV forces obtained by IDDES shown in Figure 25. Since the ratio of torsional to vertical VIVs is consistent with the modal ratio. Therefore, the coupled torsional VIVs can be determined as follow:

$$\theta_F(s) = Y_F(s) \frac{\varphi_t(s)}{\varphi_v(s)} \tag{7}$$

Where $\varphi_t(s)$ is the first torsional mode shape that shown in Figure 4(b). According to Eq. (5), the theoretical MSCF for the CCB using Scanlan nonlinear model is 1.19, while the MSCF using Scanlan linear model with/without considering span-wise correlations is 1.31 and 1.53. Figure 28 Further compares the VIVs from the section model multiplied these MSCF values, while the couple torsional VIVs are obtained using the Eq.(7). Compared to the full model, the Scanlan nonlinear model underestimates the VIVs by 6.46%, while the Scanlan linear model without span-wise correlations overestimates them by 20%. In contrast, the Scanlan linear model with span-wise correlations shows only a 2.4% deviation, accurately capturing the coupled torsional-vertical VIVs.

5. Conclusions

This paper presents an experimental and numerical study regarding the effects of superelevation and spatial curvature on VIVs of a CCB during the service stage. Fluid-structure interaction simulations using 2D URANS and 3D IDDES have been considered, aiming at explaining the flow mechanisms and assessing their capabilities in reproducing the VIV response of WTTs. Furthermore, the spatial curvature effects and the Modal shape correlation factor (MSCF) are clarified by comparing results from straight sectional and full curved model WTTs with the same geometry scale of 1:50. The conclusions are summarized as follows:

(1) CFD simulations using zero-thickness baffles effectively reduces the need for fine mesh around barriers, accelerating FSI simulations by a factor of 6.9. Regarding the FSI accuracy, 2D URANS overestimates the VIV amplitude by about 31.6% due to incorrect predictions of vortex evolution on the lower surface and the absence of spanwise correlations. In contrast, 3D IDDES significantly improves VIV simulation accuracy, with experimental deviations within 3.3%, making it suitable for the wind-resistant design for in-service CCB deck with superelevation and barriers.

(2) The analyzed CCB deck exhibits large-amplitude VIVs in two distinct lock-in regions. Superelevation increases the second lock-in VIV amplitude at a 180° yaw angle by 3.35 times compared to 0° yaw angle, mainly due to the strong secondary vortex forming downstream of the central barrier that enhances vortex-induced forces.

(3) As superelevation rate increases from 1.5% to 6%, the second lock-in VIVs at 0° yaw disappear, while VIVs at 180° increases by about 38%. It is thus shown that superelevation significantly affects the VIVs of CCBs and should be carefully considered in their designs.

(4) Coupled vertical-torsional VIVs are observed in the full curved model WTTs, with the onset speed occurring approximately 4.6 m/s earlier than straight sectional model. The experimental MSCF is 1.28, which aligns with Scanlan's linear theory when spanwise correlation is considered. By using the MSCF and mode shape ratio, coupled vertical-torsional VIVs of curved bridges can be predicted using only the results from straight sectional model, avoiding costly full curved bridge model.

Acknowledgments

The authors express their gratitude for financial support from National Key Research and

Development Program of China (2022YFC3005302), Guangxi Science and Technology Base and Talent Project (AA23026011), National Natural Science Foundation of China (52408514 & U23A20662), Natural Science Foundation of Guangxi (2025GXNSFBA069139), Guangxi Science and Technology Base and Talent Project (AD23026185), China Postdoctoral Science Foundation (2023M740786 & 2024T170188), and Innovation Project of Guangxi Graduate Education (YCSW2024060).

Data availability

The data that support the findings of this study are available from the corresponding author upon reasonable request.

Author Contributions

All authors contributed to this work.

Conflicts of Interest

The authors declare no conflict of interest.

References

[1] L. Zhu, R.K. Su, Leung, M. Li, Finite beam element with 26 DOFs for curved composite box girders considering constrained torsion, distortion, shear lag and biaxial slip, Engineering Structures, 232 (2021) 111797.
[2] B. Morais da Costa, J. Wang, J.B. Jakobsen, O.A. Øiseth, J.T. Snæbjørnsson, Bridge buffeting by skew winds: A revised theory, DOI (2021).
[3] H. Bai, N. Ji, G. Xu, J. Li, An alternative aerodynamic mitigation measure for improving bridge flutter and vortex induced vibration (VIV) stability: Sealed traffic barrier, Journal of Wind Engineering and Industrial Aerodynamics, 206 (2020).
[4] L. Zhao, F. Wu, T. Han, L. Li, T. Pan, H. Xiao, Y. Ge, Aerodynamic force distribution and vortex drifting pattern around a double-slotted box girder under vertical vortex-induced vibration, Journal of Wind Engineering and Industrial Aerodynamics, 241 (2023).
[5] R.C. Battista, M.S. Pfeil, Reduction of vortex-induced oscillations of Rio--Niteroi bridge by dynamic control devices, Journal of Wind Engineering and Industrial Aerodynamics, 84 (2000) 273-288.
[6] H. Li, S. Laima, Q. Zhang, N. Li, Z. Liu, Field monitoring and validation of vortex-induced vibrations of a long-span suspension bridge, Journal of Wind Engineering and Industrial Aerodynamics, 124 (2014) 54-67.
[7] Y. Ge, L. Zhao, J. Cao, Case study of vortex-induced vibration and mitigation mechanism for a long-span suspension bridge, Journal of Wind Engineering and Industrial Aerodynamics, 220 (2022) 104866.
[8] S. Cao, Y. Zhang, H. Tian, R. Ma, W. Chang, A. Chen, Drive comfort and safety evaluation for vortex-induced vibration of a suspension bridge based on monitoring data, Journal of Wind Engineering and Industrial Aerodynamics, 204 (2020) 104266.

[9] Y. Fu, F. Wu, C. Chai, W. Cui, Y. Li, L. Zhao, Assessment of driving safety and comfort during vortex-induced vibrations in a long-span bridge considering wind-vehicle-bridge interactions, Journal of Wind Engineering and Industrial Aerodynamics, 257 (2025) 106007.
[10] A. Larsen, S. Esdahl, J.E. Andersen, T. Vejrum, Storebælt suspension bridge–vortex shedding excitation and mitigation by guide vanes, Journal of Wind Engineering and Industrial Aerodynamics, 88 (2000) 283-296.
[11] L. Zhao, W. Cui, X. Shen, S. Xu, Y. Ding, Y. Ge, A fast on-site measure-analyze-suppress response to control vortex-induced-vibration of a long-span bridge, Structures, Elsevier, 2022, pp. 192-201.
[12] L. Liu, Y. Zou, X. He, J. Yang, Z. Wang, D. Guo, Experimental investigation on vortex-induced vibration of a long-span rail-cum-road bridge with twin separated parallel decks, Journal of Wind Engineering and Industrial Aerodynamics, 228 (2022) 105086.
[13] F. Wu, Z. Wang, L. Zhao, T. Pan, H. Xiao, Y. Ge, Aerodynamic force distribution characteristics around a double-slotted box girder of a long-span bridge during vortex-induced vibration, Journal of Bridge Engineering, 28 (2023) 04022132.
[14] E. Lopez-Nuñez, M. Ogueta-Gutiérrez, O. Gómez-Ortega, R. Manzanares-Bercial, E. Roibás-Millán, S. Franchini, Effect of wind barriers on the aeroelastic instabilities of a hinged-deck cross-section cable-stayed bridge, Engineering Structures, 287 (2023) 116112.
[15] B. Wu, S. Laima, Experimental study on characteristics of vortex-induced vibration of a twin-box girder and damping effects, Journal of Fluids and Structures, 103 (2021) 103282.
[16] Y. Tamura, P. Van Phuc, Development of CFD and applications: Monologue by a non-CFD-expert, Journal of Wind Engineering and Industrial Aerodynamics, 144 (2015) 3-13.
[17] Y. Tang, Y. Hui, K. Li, LES study on variation of flow pattern around a 4: 1 rectangular cylinder and corresponding wind load during VIV, J Wind Eng Ind Aerod, 228 (2022) 105121.
[18] C. Wang, Z. Huang, X. Hua, X. He, S. Zhou, Z. Chen, Aerodynamic mechanism of triggering and suppression of vortex-induced vibrations for a triple-box girder, Journal of Wind Engineering and Industrial Aerodynamics, 227 (2022) 105051.
[19] Y. Song, Z. Ti, H. Deng, Y. Li, Vortex-induced vibrations of sea-crossing bridge deck subject to dynamic wave boundary layer airflows, Physics of Fluids, 37 (2025).
[20] B.D.S. AASHTO, American Association of State Highway and Transportation Officials, Washington, DC, 4 (2010).
[21] B. Wu, S. Li, K. Li, L. Zhang, Numerical and experimental studies on the aerodynamics of a 5: 1 rectangular cylinder at angles of attack, Journal of Wind Engineering and Industrial Aerodynamics, 199 (2020) 104097.
[22] H. Bai, R. Li, G. Xu, A. Kareem, Aerodynamic performance of Π-shaped composite deck cable-stayed bridges including VIV mitigation measures, Journal of Wind Engineering and Industrial Aerodynamics, 208 (2021) 104451.
[23] Y. Yang, R. Zhou, Y. Ge, L. Zhang, Experimental studies on VIV performance and countermeasures for twin-box girder bridges with various slot width ratios, Journal of Fluids and Structures, 66 (2016) 476-489.
[24] Q. Duan, C. Ma, T. Zhang, Z. Li, Vortex-induced vibration characteristic and trigger mechanism of semi-closed streamlined box girder trans-sea bridges, Ocean Engineering, 312 (2024) 119053.
[25] B. Ge, R. Ma, F. Li, X. Hu, A. Chen, Probabilistic vortex-induced vibration occurrence prediction of the twin-box girder for long-span cable-stayed bridges based on wind tunnel tests, Engineering Structures, 262 (2022) 114325.
[26] T. Zhang, Y. Sun, M. Li, X. Yang, Experimental and numerical studies on the vortex-induced vibration of two-box edge girder for cable-stayed bridges, Journal of wind engineering and industrial aerodynamics, 206 (2020) 104336.
[27] D. Zeng, C. Ma, C. Pei, Y. Xu, Vortex-induced vibration characteristic in two regions of double deck plate-truss composite girder and countermeasure study, Structures, Elsevier, 2025, pp. 107946.
[28] Q. Duan, J. Shang, C. Ma, Z. Li, Vortex-induced vibration characteristics of twin-box girder section in long-span

bridge: A numerical evaluation method, Physics of Fluids, 37 (2025).
[29] J. Wang, C. Ma, M. Li, N. Yeung, S. Li, Experimental and numerical studies of the vortex-induced vibration behavior of an asymmetrical composite beam bridge, Advances in Structural Engineering, 22 (2019) 2236-2249.
[30] L. Liu, Y. Zou, X. He, J. Yang, X. Zhou, Z. Wang, Effect of spacing on Vortex-induced vibration performances for rail-cum-road bridges with twin asymmetric parallel decks, Structures, Elsevier, 2024, pp. 106749.
[31] L. Liu, Y. Zou, X. He, J. Yang, Z. Wang, D. Guo, Experimental investigation on vortex-induced vibration of a long-span rail-cum-road bridge with twin separated parallel decks, Journal of Wind Engineering and Industrial Aerodynamics, 228 (2022).
[32] L. Liu, Y. Zou, X. He, X. Zhou, C. Cai, J. Yang, Effects of wind barriers on VIV performances of twin separated parallel decks for a long-span rail-cum-road bridge, Journal of Wind Engineering and Industrial Aerodynamics, 236 (2023) 105367.
[33] S. Stoyanoff, P.-O. Dallaire, Z. Taylor, G. Larose, Aerodynamic problems of parallel deck bridges, Bridge Structures, 15 (2019) 139-147.
[34] A.M. Marra, C. Mannini, G. Bartoli, Wind tunnel modeling for the vortex-induced vibrations of a yawed bridge tower, Journal of Bridge Engineering, 22 (2017) 04017006.
[35] S. Laima, H. Li, W. Chen, J. Ou, Effects of attachments on aerodynamic characteristics and vortex-induced vibration of twin-box girder, Journal of Fluids and Structures, 77 (2018) 115-133.
[36] C. Hu, L. Zhao, Y. Ge, Multiple-order vertical vortex-induced vibration mechanism of a typical streamlined closed-box girder, Journal of Wind Engineering and Industrial Aerodynamics, 227 (2022).
[37] T. Zhang, Y. Sun, Y. Lei, M. Li, M. Li, H. Liao, Vortex-induced vibration of a flexible rectangular cylinder: Experimental investigation and comparative study of theoretical models, Journal of Wind Engineering and Industrial Aerodynamics, 220 (2022).
[38] A.M. Marra, C. Mannini, G. Bartoli, Measurements and improved model of vortex-induced vibration for an elongated rectangular cylinder, Journal of Wind Engineering and Industrial Aerodynamics, 147 (2015) 358-367.
[39] X. Chen, C. Zhu, C. Ma, Q. Li, Vortex-induced vibration of twin-box girder and its aerodynamic characteristics study based on high-order dynamic decomposition, Journal of Wind Engineering and Industrial Aerodynamics, 249 (2024).
[40] S. Xu, G. Fang, O. Øiseth, L. Zhao, Y. Ge, Experimental study on distributed aerodynamic forces of parallel box girders with various slot width ratios and aerodynamic countermeasures during vortex-induced vibration, Journal of Wind Engineering and Industrial Aerodynamics, 240 (2023) 105493.
[41] S. Avila-Sanchez, O. Lopez-Garcia, A. Cuerva, J. Meseguer, Characterisation of cross-flow above a railway bridge equipped with solid windbreaks, Engineering Structures, 126 (2016) 133-146.
[42] Q. Duan, C. Ma, H. Yang, Influence of non-uniform grid plates on the vortex-induced vibration performance of twin-box girder section, Structures, 58 (2023).
[43] Z. Wang, Z. Zhang, VIV properties of π-shaped bridge sectional model: dependence on torsional-bending frequency ratio, Journal of Bridge Engineering, 26 (2021) 06021003.
[44] L. Zhao, Z. Wang, G. Fang, W. Cui, K. Li, Y. Ge, Vortex-induced vibration control of 5: 1 rectangular cylinder with an attached active splitter plate based on open-loop control method, Physics of Fluids, 37 (2025).
[45] Q. Wang, S. Yang, L. Huang, F. Wang, F. Chu, The vortex-induced vibration performance of railway rectangular box girders, Physics of Fluids, 37 (2025).
[46] Y. Su, M. Li, J. Di, R. Sun, M. Li, F. Qin, Y. Jiang, J. Wang, Scale effects on buffeting response of long-span bridges, Engineering Structures, 341 (2025) 120862.
[47] A.J. Álvarez, F. Nieto, Correlation and modal analysis techniques for the study of the VIV response of a twin-box deck based on 3D LES simulations, Meccanica, DOI 10.1007/s11012-024-01774-6(2024).

[48] A.J. Álvarez, F. Nieto, D.T. Nguyen, J.S. Owen, S. Hernández, 3D LES simulations of a static and vertically free-to-oscillate 4:1 rectangular cylinder: Effects of the grid resolution, Journal of Wind Engineering and Industrial Aerodynamics, 192 (2019) 31-44.
[49] M.W. Sarwar, T. Ishihara, Numerical study on suppression of vortex-induced vibrations of box girder bridge section by aerodynamic countermeasures, Journal of Wind Engineering and Industrial Aerodynamics, 98 (2010) 701-711.
[50] X. Wang, F. Xu, Z. Zhang, Y. Wang, M. Zhang, Numerical explorations of the vortex-induced vibration of a streamlined box girder with water-filled barriers, Journal of Wind Engineering and Industrial Aerodynamics, 240 (2023).
[51] J. Zhang, W. Wang, C. Wang, X. Hua, Z. Huang, Numerical investigation on vertical vortex-induced vibrations of triple-box girders with curved and linear-type webs, Journal of Wind Engineering and Industrial Aerodynamics, 242 (2023).
[52] Z. Zhang, F. Xu, Y. Wang, X. Wang, Fluid-structure interaction analysis of a 4: 1 rectangular prism undergoing vortex-induced vibration, Journal of Wind Engineering and Industrial Aerodynamics, 254 (2024) 105918.
[53] J. Li, B. Wu, C. Ma, B. Cui, S. Li, Flow patterns and vortex related characteristics of tandem rectangular structures with recessed corners, Physics of Fluids, 37 (2025).
[54] H. Xiao, Z. Liu, Z. Chen, R. Qing, C. Wang, Numerical and Experimental Investigation on Vortex-Induced Vibration Suppression of a Self-Anchored Suspension Bridge with a Central-Slotted Box Girder, Journal of Bridge Engineering, 30 (2025) 04024106.
[55] J. Dong, Q. Wang, Y. Qiu, L. Huang, H. Liao, Suppression efficiency of the maintenance rail position and guide vanes on vortex-induced vibrations of a streamlined closed-box girder, Physics of Fluids, 37 (2025).
[56] L. Huang, Q. Wang, H. Liao, Effective wind fairing combination aerodynamic measures against vortex-induced vibrations of Π-shaped composite bridge decks, Physics of Fluids, 37 (2025).
[57] F. Wu, Z. Wang, L. Zhao, T. Pan, H. Xiao, Y. Ge, Aerodynamic Force Distribution Characteristics around a Double-Slotted Box Girder of a Long-Span Bridge during Vortex-Induced Vibration, Journal of Bridge Engineering, 28 (2023).
[58] Y. Ge, L. Zhao, J. Cao, Case study of vortex-induced vibration and mitigation mechanism for a long-span suspension bridge, Journal of Wind Engineering and Industrial Aerodynamics, 220 (2022).
[59] L. Liu, J. Yang, Y. Zou, X. He, C. Cai, Effects of wind barriers on the aerodynamic characteristics of twin-separated parallel decks for a long-span rail-cum-road bridge, Advances in Structural Engineering, 26 (2023) 2963-2983.
[60] D. Xin, J. Zhan, H. Zhang, J. Ou, Control of vortex-induced vibration of a long-span bridge by inclined railings, Journal of Bridge Engineering, 26 (2021) 04021093.
[61] D. Xia, L. Dai, L. Lin, Experimental study on the effect of attachments on the vortex-induced vibration of a centrally slotted box deck, Journal of Applied Fluid Mechanics, 16 (2023) 1119-1133.
[62] B. Nicese, A.M. Marra, G. Bartoli, C. Mannini, VIV mechanisms of a non-streamlined bridge deck equipped with traffic barriers, Journal of Fluids and Structures, 132 (2025) 104195.
[63] Y. Yan, T. Yagi, K. Noguchi, Y. Ito, R. Shimada, Effects of handrail details on vortex-induced vibration for a Box-girder bridge, Journal of Bridge Engineering, 27 (2022) 04021114.
[64] Y. Yang, L. Li, G. Yao, M. Wang, C. Zhou, T. Lei, H. Tan, Study on the influence of the fully enclosed barrier on the vortex-induced vibration performance of a long-span highway–railway double-deck truss bridge, Physics of Fluids, 36 (2024).
[65] H. Yang, S. Zheng, C. Ma, Vertical vortex-induced vibration performance of split triple-box girders with various ancillary facility configurations, Physics of Fluids, 37 (2025).
[66] T. Yoshimura, Y. Mizuta, F. Yamada, H. Umezaki, T. Shinohara, N. Machida, T. Tanaka, T. Harada, Prediction of vortex-induced oscillations of a bridge girder with span-wise varying geometry, Journal of Wind Engineering and Industrial Aerodynamics, 89 (2001) 1717-1728.

[67] S. Liu, L. Zhao, G. Fang, C. Hu, Y. Ge, Investigation on aerodynamic force nonlinear evolution for a central-slotted box girder under torsional vortex-induced vibration, Journal of fluids and structures, 106 (2021) 103380.
[68] M. Xu, L. Patruno, S. de Miranda, A pressure–velocity jump approach for the CFD modelling of permeable surfaces, Journal of Wind Engineering and Industrial Aerodynamics, 233 (2023) 105317.
[69] Z. Liu, F. He, M. Li, H. Xiao, Z. Wei, A. Yan, Z. Chen, Aerodynamic interference mechanism of vertical vortex-induced vibration of a ∏-shaped girder paralleled with a truss girder, Structures, 58 (2023).
[70] L. Huang, J. Dong, Q. Wang, H. Liao, M. Li, Investigation of vortex-induced vibration of a Π-type bridge girder and its suppression using G-shaped apron combination measure, Physics of Fluids, 36 (2024).
[71] Z. Liu, F. He, A. Yan, Z. Liu, T. Yin, Z. Chen, Mechanism and Aerodynamic Countermeasures of Vortex-Induced Vibration of a Cable-Stayed Bridge with Narrow Π-Shaped Girder Sections, Journal of Bridge Engineering, 28 (2023) 04023090.
[72] B.M. da Costa, J. Wang, J.B. Jakobsen, J. þór Snæbjörnsson, O.A. Øiseth, Long-term response of a curved floating bridge to inhomogeneous wind fields, Journal of Wind Engineering and Industrial Aerodynamics, 240 (2023) 105488.
[73] J. Wang, J.B. Jakobsen, O.A. Øiseth, J.T. Snæbjørnsson, Bridge buffeting by skew winds: A quasi-steady case study, DOI (2022).
[74] Z. Wang, J.B. Jakobsen, Y. Sha, Sensitivity analysis of numerical modeling approaches for curved floating bridge buffeting response, Ocean Engineering, 325 (2025) 120478.
[75] B. Wang, M. Zhang, F. Xu, Experimental investigation on the vortex-induced vibration of a rectangular 4: 1 cylinder under skew winds, Journal of Wind Engineering and Industrial Aerodynamics, 229 (2022) 105114.
[76] X. Wang, F. Xu, Z. Zhang, Y. Wang, Numerical simulation of the vortex-induced vibrations of a 4:1 rectangular cylinder subjected to yaw uniform currents, Journal of Wind Engineering and Industrial Aerodynamics, 252 (2024).
[77] Z. Xie, X. He, H. Wang, Z. Huang, H. Li, Aerodynamic characteristics of a high-speed train on flat-box girder for different yaw angles, Journal of Wind Engineering and Industrial Aerodynamics, 250 (2024) 105759.
[78] P. Irwin, Full aeroelastic model tests, Aerodynamics of Large Bridges, Routledge2017, pp. 125-135.
[79] G. Larose, A. Davenport, J. King, Wind effects on long span bridges: Consistency of wind tunnel results, Journal of Wind Engineering and Industrial Aerodynamics, 42 (1992) 1191-1202.
[80] G. Diana, G. Fiammenghi, M. Belloli, D. Rocchi, Wind tunnel tests and numerical approach for long span bridges: The Messina bridge, Journal of Wind Engineering and Industrial Aerodynamics, 122 (2013) 38-49.
[81] Z. Wang, J. Zhu, C. Wen, Z. Zhang, Multi-mode vortex-induced vibrations characteristics based on a full bridge aeroelastic model, Physics of Fluids, 37 (2025).
[82] Z. Zhang, Y. Ge, Z. Chen, Vortex-induced oscillations of bridges: theoretical linkages between sectional model tests and full bridge responses, Wind & structures, 19 (2014) 233-247.
[83] F. Ehsan, R.H. Scanlan, Vortex-induced vibrations of flexible bridges, Journal of Engineering Mechanics, 116 (1990) 1392-1411.
[84] J.H. Macdonald, P.A. Irwin, M.S. Fletcher, Vortex-induced vibrations of the Second Severn Crossing cable-stayed bridge—full-scale and wind tunnel measurements, Proceedings of the Institution of Civil Engineers-Structures and Buildings, 152 (2002) 123-134.
[85] S. Zhou, X. Hua, Z. Chen, W. Chen, Experimental investigation of correction factor for VIV amplitude of flexible bridges from an aeroelastic model and its 1: 1 section model, Engineering Structures, 141 (2017) 263-271.
[86] M.S. Gritskevich, A.V. Garbaruk, J. Schütze, F.R. Menter, Development of DDES and IDDES formulations for the k-ω shear stress transport model, Flow, turbulence and combustion, 88 (2012) 431-449.
[87] X. Lin, J. Zhang, J. Zheng, S. Liu, Performance and wake interaction between two aligned vertical axis turbines, Ocean Engineering, 292 (2024) 116478.

[88] J. Niu, Y. Zhang, R. Li, Z. Chen, H. Yao, Y. Wang, Aerodynamic simulation of effects of one-and two-side windbreak walls on a moving train running on a double track railway line subjected to strong crosswind, Journal of Wind Engineering and Industrial Aerodynamics, 221 (2022) 104912.
[89] K. He, X. Su, G. Gao, S. Krajnović, Evaluation of LES, IDDES and URANS for prediction of flow around a streamlined high-speed train, Journal of Wind Engineering and Industrial Aerodynamics, 223 (2022) 104952.
[90] M. Xu, L. Patruno, Y.-L. Lo, S. de Miranda, Simulation strategies for wind shields and porous barriers for bridge deck optimization, Structures, 40 (2022) 824-839.
[91] AASHTO, A policy on geometric design of highways and streets, American Association of State Highway and Transportation Officials: Washington, DC, USA, DOI (2018).
[92] S. Li, R. Wan, D. Wang, P. Guo, Effect of end plates on transiting test for measuring the aerodynamic coefficient of structures using wind generated by a moving vehicle, J Wind Eng Ind Aerod, 190 (2019) 273-286.
[93] C. Wang, Q. Wen, S. Zhou, X. Hua, Z. Huang, Z. Chen, Effects of end condition and aspect ratio on vortex-induced vibration of a 5: 1 rectangular cylinder, Journal of Fluids and Structures, 109 (2022) 103480.
[94] A. Buljac, H. Kozmar, S. Pospil, M. Machek, Flutter and galloping of cable-supported bridges with porous wind barriers, Journal of Wind Engineering and Industrial Aerodynamics, 171 (2017) 304-318.
[95] M. Xu, L. Patruno, Y.-L. Lo, S. de Miranda, Simulation strategies for wind shields and porous barriers for bridge deck optimization, Structures, 2022, pp. 824-839.
[96] M.C. Montoya, J.P.C. King, L. Kong, F. Nieto, S. Hernndez, A method for improving the dynamic response of full bridge reduced-scale models in aeroelastic wind tunnel tests by using optimization algorithms, Journal of Wind Engineering and Industrial Aerodynamics, 167 (2017) 198-216.
[97] L. Bruno, M.V. Salvetti, F. Ricciardelli, Benchmark on the Aerodynamics of a Rectangular 5:1 Cylinder: An overview after the first four years of activity, Journal of Wind Engineering and Industrial Aerodynamics, 126 (2014) 87-106.
[98] P. Zou, S. Cao, J. Cao, Spanwise correlation and coherent structures of separated flow around rectangular 5: 1 cylinder, Journal of Wind Engineering and Industrial Aerodynamics, 231 (2022) 105211.
[99] Z. Zhang, F. Xu, Spanwise length and mesh resolution effects on simulated flow around a 5: 1 rectangular cylinder, Journal of Wind Engineering and Industrial Aerodynamics, 202 (2020) 104186.
[100] F.R. Menter, M. Kuntz, R. Langtry, Ten years of industrial experience with the SST turbulence model, Turbulence, heat and mass transfer, 4 (2003) 625-632.
[101] E. Robertson, V. Choudhury, S. Bhushan, D.K. Walters, Validation of OpenFOAM numerical methods and turbulence models for incompressible bluff body flows, Computers & Fluids, 123 (2015) 122-145.
[102] A.J.Á. Naveira, Simulation of vortex shedding and vortex induced vibrations in multibox bridge decks using CFD, Universidade da Coruña, 2019.
[103] A. Dullweber, B. Leimkuhler, R. McLachlan, Symplectic splitting methods for rigid body molecular dynamics, The Journal of chemical physics, 107 (1997) 5840-5851.
[104] M. Alletto, Comparison of overset mesh with morphing mesh: flow over a forced oscillating and freely oscillating 2D cylinder, OpenFOAM® Journal, 2 (2022) 13-30.
[105] M.o. Transportation, C.o. PRC, JTG/T 3360–01–2018 Wind-Resistant Design Specification for Highway Bridges, China Communications Press Co., Ltd. Beijing, China, 2018.
[106] N. Shiraishi, M. Matsumoto, On classification of vortex-induced oscillation and its application for bridge structures, Journal of Wind Engineering and Industrial Aerodynamics, 14 (1983) 419-430.
[107] C. Shang, H. Xiang, Y. Bao, Y. Li, K. Luo, Mechanism of vortex-induced vibration in two lock-in regions for truss girder sections, Journal of Wind Engineering and Industrial Aerodynamics, 255 (2024) 105946.
[108] L. Bruno, D. Fransos, N. Coste, A. Bosco, 3D flow around a rectangular cylinder: A computational study, Journal

719 of Wind Engineering and Industrial Aerodynamics, 98 (2010) 263-276.
720 [109] L. Patruno, M. Ricci, S. de Miranda, F. Ubertini, Numerical simulation of a 5: 1 rectangular cylinder at non-null
721 angles of attack, Journal of Wind Engineering and Industrial Aerodynamics, 151 (2016) 146-157.
722 [110] J. Kou, W. Zhang, An improved criterion to select dominant modes from dynamic mode decomposition, European
723 Journal of Mechanics-B/Fluids, 62 (2017) 109-129.
724 [111] M. Kiewat, Streaming modal decomposition approaches for vehicle aerodynamics, Technische Universität München,
725 2019.
726 [112] G. Min, N. Jiang, Data-driven identification and pressure fields prediction for parallel twin cylinders based on POD
727 and DMD method, Physics of Fluids, 36 (2024).
728 [113] Y. Sun, M. Li, M. Li, H. Liao, Spanwise correlation of vortex-induced forces on typical bluff bodies, Journal of
729 Wind Engineering and Industrial Aerodynamics, 189 (2019) 186-197.
730 [114] F. Ricciardelli, Effects of the vibration regime on the spanwise correlation of the aerodynamic forces on a 5: 1
731 rectangular cylinder, Journal of Wind Engineering and Industrial Aerodynamics, 98 (2010) 215-225.
732